Development of multifunctional hybrid metal/carbon composite structures

F. Pinto, F.Rizzo, M. Meo

Material Research Centre, Department of Mechanical Engineering,

University of Bath, Bath, UK

ABSTRACT

*The aim of this work is to design, manufacture and test a hybrid composite by embedding optimised copper or Shape Memory Alloy (SMA) wires within carbon fibre laminate for improved impact resistance, intrinsic strain sensing and impact detection capability, non-destructive testing and de-icing functionalities. It was demonstrated that with an appropriate optimisation of the wires a reduction of damaged area was experienced. It was shown that the hybrid network can work as a strain sensor by monitoring the variation of its electrical resistance under load and to identify the presence of a localised load such as an impact event. Then, non-destructive capability for assessing defects was shown where by applying an electrical current to the metal wires, heat was generated and distortion of the thermal field due to a damaged area was measured using a Step Heating Thermography (SHT) process, creating an image of the damage. De-icing operations was presented by exploiting the Joule effect where the local temperature increase was able to melt down an ice layer and hence avoid aerodynamic variation of aircraft surfaces. The results showed that the multifunctionality of this embedded smart material can improve the safety and reliability of aircraft structures and reduce maintenance costs.*Keywords: Multifunctional, impact, SHM, NDT, de-icing

1. Introduction

In modern aerospace and automotive industry, Carbon Fibres Reinforced Polymers (CFRP) are largely used for structural applications due to the combination between their specific mechanical properties and low weight. In particular, along the in-plane direction, specific strength and mechanical properties result to be very high, however, because of their intrinsic layered structure, in the through-the-thickness direction, the material shows weak mechanical resistance. As a consequence, composite laminates are susceptible to inter-laminar delamination if subjected to Low-Velocity Impacts (LVIs) that could lead to structure failures. This is widely reported by Abrate [1] in his comprehensive review on composite materials under impact conditions. Over the last two decades, a large amount of research works has been presented and a series of possible solutions have been developed in order to overcome these structural weaknesses. Russel et al. [2-4] modified the matrix toughness in order to achieve global mechanical properties increase, while Tessington and Yaun [5, 6] chose to reinforce carbon fibres-matrix chemical bonding to reach the same properties benefits. The use of design alternatives such as the use of stiches along the thickness direction resulted also to be effective [7-9] as well as the inclusion of +45/-45° woven fabrics [10, 11] within the laminate's stacking. Other researchers followed a different approach embedding together more than a single array of reinforcement leading to a "hybridisation" of the composite material. Bunsell and Naik [12, 13] studied the mechanical behaviour of laminates obtained by laying up both carbon and glass fibres observing an improvement of fracture toughness, impact strength, notch sensitivity and manufacturing costs in respect with a traditional CFRP laminate, but a higher total weight due

to higher glass fibres density. Marom et al. [14] suggested a combination of carbon and Kevlar fibres as polymer reinforcement, obtaining an improved fatigue response but reduced stiffness. A very popular solution was the use of Fibre-Metal Laminates (FMLs) such as ARALL[15, 16] and GLARE[17, 18] that showed interesting corrosive resistance, fatigue and impact damage tolerance but higher manufacturing costs. Several researchers focused their attention on the study of the interaction between metal wires and CFRP: Bradley et al. [19] studied the effective benefits of hybridisation for mechanical properties, verifying the impact properties increase when metal wires are located close to the impacted area. Other works that exploit the unique physical properties of Shape Memory Alloys (SMAs) are focused on the use of SMAs wires as secondary reinforcement. In this context, Paine [20] showed impact resistance increase placing wires in the tensile portion of laminate where martensitic phase transformation generates a plateau region in the stress-strain curve, leading to a hysteresis behaviour where part of energy is dissipated, unlike other metal wires cases. Such behaviour can be exploited to absorb more impact energy during a LVI event. The metal wires enclosed inside the CFRP's stacking sequence, not only may be used for mechanical purposes, but also to activate additional non-structural abilities.

In particular, the use of the metal reinforcement system can be exploited to set-up a smart network system that allows to carry out an in-situ Structural Health Monitoring (SHM) in order to increase the safety level of the structure and avoid the use of external devices during security control and maintenance procedures. Hence, the hybridisation process not only can increase the mechanical resistance improvement, but the same smart material can be exploited to perform a continuous structural integrity monitoring. Hence, a multifunctional composite where both structural (mechanical properties) and non-structural properties (SHM) can be improved by embedding a metallic phase into a polymeric composite material. A real time monitoring of structural health can be achieved by evaluating through electric resistance measurements, the strain distribution over the laminate, and therefore detect a critical load, its exact position, creating an impact detection system. In particular, Abry et al. [21] showed that carbon fibres could act as electric conductors embedded in an insulating matrix. In particular, by performing a resistance measurement during a post-buckling test, they demonstrated the possibility to detect inner defects in the structure but not their exact positions. Schulte et al. [22] reported the possibility to detect the propagation of several typologies of damage inside the CFRP during static or fatigue loading by monitoring the electrical resistivity of CFRP since fibre breakage decreases the resistivity value. Resistivity dependence from temperature, fibre volume fraction, applied load and stacking sequence is also evaluated and reported in the study. However, several issues were observed using carbon fibres as damage detection material such as difficulties in the connection between the sample and the measuring instrumentation and high fragility of carbon fibres. Other researchers, investigated the resistance variation of metal wires embedded within CFRP.

Cui et al. [23] illustrated the mathematical model on the relationship between strain and electrical resistance in a SMA and showed that the relationship is linear and temperature-independent. Nagai et al. [24] presented experimentally the strain sensing ability of SMA wires embedded within CFRP through a tensile test, confirming strain-resistance linear dependence and temperature-independence for martensitic SMA structure. Then the smart reinforcement allowed to analyse the structural integrity of the material once an impact event or damage has occurred. There are different techniques to achieve this objective but over the last decades, among Non Destructive Techniques (NDTs), Infrared (Ir) thermography resulted reliable in detecting sub-surface damage distribution for both metal and composite parts [25]. The technique is based on monitoring the apparent temperature gradient which is captured on a sample's surface after a heat stimulus is applied. Since the heat diffusion rate of a damaged

area differs from an integer one, the heat wave propagation is modified by the presence of cracks or delamination. Traditionally, different external heat sources are used to generate the heat stimulus such as high power photographic flashes [26] or radiators [27] that represent a large limitation of the technique, which results not cost effective and suitable only on large scale applications. Recently, some researchers chose to remove the use of external devices exploiting different solutions to increase the temperature of the laminate from the inside in order to develop what has been called "material enabled" thermography. Suzuki et al. [28] carried out an experimental campaign in which by heating the carbon fibres of an impacted CFRP using an electric current, it was possible to measure the presence of a damaged area due to the increased fibre-fibre contact points generated by the presence of the indentation. Amhed [29] and Orłowska[30] illustrated the possibility to exploit the presence of an additional embedded component as internal heat source. In [29] a "heat emitting layer" within the laminate stack was embedded , applying an electrical current, a thermal wave was generated, whose propagation through the thickness was used to inspect the sample's integrity. Finite elements simulations were performed to predict the behaviour of the heat wave propagation over damaged areas showing good agreement with the experimental results. However, the insert of these additional layers generates a discontinuity into sample's structure with a local change of mechanical properties. In [30], a 3-D resistive structure was embedded inside the CFRP by drilling the sample. Applying a small current, it was possible to heat the composite along all its directions and to record thermal signals of potential inner defects, even if several manufacturing issues were observed during laminate fabrication because of the drilling tolerance and the presence of holes inside the laminate structure (loss of mechanical properties).

We demonstrate that it is also possible to use the same instrumentation to fulfil another relevant issue in aircraft operations: the de-icing procedure. During the aircraft operative service, the extreme environmental condition (-30/-50 °C) leads to ice growth on wings surfaces. These ice conglomerates can change the geometry of the aerodynamic profile causing a series of potentially critical issues such as unwanted vibrations, loss of aircraft control and in eventually, the total loss of aerodynamic on the wings. In order to avoid this issue, several solutions have been adopted over the years such as mechanical pneumatic systems [31], acoustical systems [32] and electromagnetic pulsing systems [33]. In particular, thermal solutions are largely employed in the modern aircraft industry. The heating of a conductor by Joule effect results very effective in dissolving ice formations, by locally increasing the temperature on the interested part. Different techniques were developed: create short-circuiting condition on conductors [34], apply Eddy-current in AC [35] and use thermoresistive layers which are applied on the top of existing layers [36]. The use of hybrid composite parts may offer another solution to solve this issue. The embedded SMA wires, if used as a heat source, can dissolve ice on interested surface and consequently, avoid external interventions or the use of complex de-icing mechanisms [37]. Indeed, since the hybrid system is able to generate a large amount of localised heat during damage analysis, it is possible to prevent ice formation on aerodynamics part exploiting the temperature increase on the external surface. In the study of advanced multifunctional materials, a particular mention needs to be made for the use of nanomaterials in fabricating multifunctional composite systems. Chien et al. [38] studied the electrical conductivity and Joule heating of polyacrylonitrile/carbon nanotube composite fibers demonstrating their monitoring and thermo-resistive enhanced features, while Kernin et al. [39] investigated the mechanical, thermal and electrical properties of an epoxy-based nanocomposite when a network of reduced graphene oxide was used as nanofiller. Good electrical conductivity and mechanical properties increase were reported with the possibility to use the material as a strain sensor. Zhang et al. instead [39] studied the use of graphene nano-

plates in glass fibre/epoxy composite to obtain an increment in mechanical properties and the possibility to use the same system as monitoring network and Joule heating de-ice system without the necessity of external devices. However, this solution has several issues in transposing the laboratory prototype to the industrial production due to the intrinsic complexity of nanomaterials and their costs.

The aim of this research work is to obtain an optimised embodiment of metal wires within traditional CFRP creating a Multifunctional composites in which the hybrid phase not only works as an additional reinforcement but is also able to enable new additional features by exploiting its thermo-electrical properties [40]. This work presents the design, manufacturing and testing of a hybrid laminate (H-CFRP) in which the hybridisation is obtained by including an array of Shape Memory Alloys or Copper wires within the laminate stacking sequence for multifunctional purposes. In the paper, the manufacturing procedures used to fabricate all the investigated samples are presented in Section 2 while the experimental set-up and testing methods for impact, sensing, Ir damage detection and de-icing tests are described in Section 3. In Section 4, results and discussions for all the aforementioned testing cases are reported whilst Section 5 includes a results summary and conclusions.

-

2. Samples Manufacturing

In order to understand the benefits of embedding metal wires inside a CFRP laminates, a series of hybrid samples were manufactured. Using a M21-T800 prepreg system, the samples were cured in autoclave at 180 °C and 100 Psi with a ramp of 0.2°C/min for 2 hours. Two different categories of samples were produced: plates to test hybrid material improvement and complex parts to test the reliability of the hybrid composite concept on proper aeronautical structures. Plates were laminated using different stacking sequences and were cut 150 mm in length, 100 mm in width and around 2 mm in thickness, while the complex parts (leading edge geometry) were manufactured using 12 layer of prepreg obtaining 130 mm of height, 150 mm of length, 120 mm of depth and 2.91 mm of average thickness (Figure 1). Copper wires (0.15 mm diameter) and Shape Memory Alloy (SMA) Nitinol (0.2 mm of diameter) were embedded at different depths within the CFRP with an inter-wires distance of 16.5 mm. In order to obtain an optimal bonding between metal wires and composite matrix (epoxy resin), SMA and copper wires were treated using two different methods. SMA surface was treated using a 10% NaOH anodic oxidation to modify the surface and increase the bonding strength between SMA and resin [41, 42]. Copper wires, instead, were treated using sand paper to increase the roughness of the metal surface and then its bonding strength with epoxy matrix [43]. Bottom W (Figure 1.a) and Top W (Figure1.b) configurations were fabricated inserting copper wires (global weight increase of ~1%) respectively between the first and the second ply (9 layers in total) from the bottom of the laminate and between the eighth and ninth ply, in order to evaluate the increase of impact properties in reference with a traditional CFRP (Figure 1.c) (Ref). Sens Cu (Figure 1.d) and Sens SMA (Figure 1.e) samples were produced by inserting copper and SMA wires respectively between the third and fourth ply (7 layers in total) in order to test the impact localisation and sensing ability of the smart embedded system.

Characterised by the presence of a Polytetrafluoroethylene (PTFE) patch inserted between the sixth and seventh ply, Therm PTFE (Figure 1.f) was fabricated using the same stacking sequence of previous samples in order to simulate a damaged area and to validate the feasibility of the Ir technique. In the Leading Edge PTFE (Figure 1.g), together with an array of SMA wires (fifth and sixth ply), a PTFE patch was inserted between the ninth and tenth ply to simulate a delaminated area in a real aerodynamic part. Leading Edge SMA (Figure 1.h),

instead, was produced using a double array of SMA wires between the fourth-fifth plies and ninth-tenth plies in order to evaluate the possibility to detect real defective areas inside a complex structure using the same Ir technique. A detailed description of samples denomination and layup is reported in Table 1.

Table 1-Manufactured samples specs. (w: wires; p: PTFE patch)

Label	Number of samples	N° Plies	Aim	Wires	Lamination sequence
Bottom W	3	9	Impact/Damage detection	Copper	[0/w/90/0/90/0/90/0/90/0]
Top W	3	9	Impact/Damage detection	Copper	[0/90/0/90/0/90/0/90/w/0]
Ref	3	9	Impact	No Wires	[0/90/0/90/0/90/0/90/0]
Sens Cu	1	7	Sensing	Copper	[0/90/0/w/90/0/90/0]
Sens SMA	1	7	Sensing	SMA	[0/90/0/w/90/0/90/0]
Therm PTFE	1	7	Damage detection	SMA + PTFE	[0/90/0/w/90/0/90/p/0]
Leading Edge PTFE	1	12	Damage detection	SMA+ PTFE	[0/0/0/0/0/w/0/0/0/0/p/0/0/0]
Leading Edge SMA	1	12	Impact/ Damage detection	SMA	[0/0/0/0/0/w/0/0/0/0/w/0/0/0]

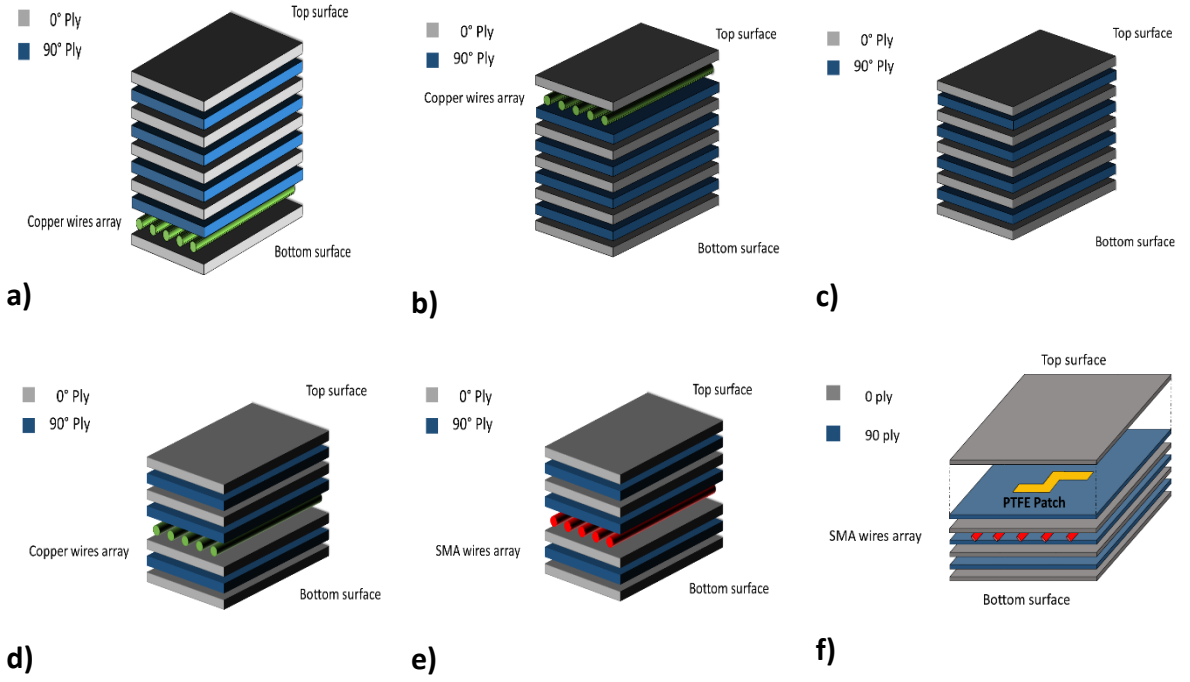

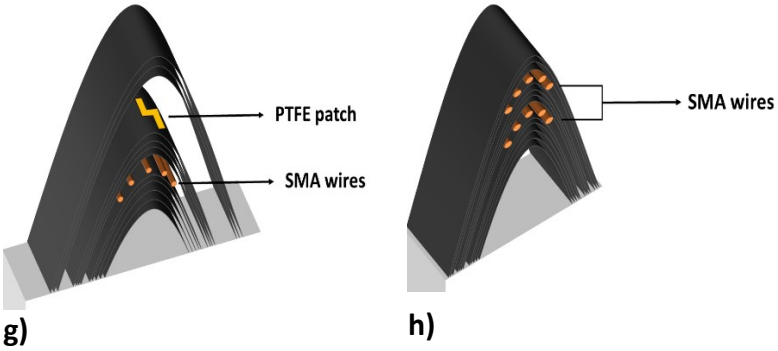

Figure 1-Stratification layout of manufactured samples: a) Bottom W (Copper wires far from impacted surface); b) Top W (Copper wires close to impacted surface); c) Ref (no wires); d) Sens Cu (copper wires-sensing); e) Sens SMA (SMA wires-sensing); f) Therm PTFE (SMA wires + PTFE patch-thermography; g) Leading Edge PTFE (leading edge-SMA wires+ PTFE patch-thermography); h) Leading Edge SMA (Leading edge -Double SMA wires-Thermography).

3. Experimental set-up

3.1 Impact Campaign

A drop tower machine was used to perform Low-Velocity Impact (LVI) tests on the samples. The impact load is applied using a hemispherical tip (20 mm of diameter) of hardened steel dropped from a height of 0.20 m with a total impactor mass of 12.864 Kg. The applied impact energy was 25J. A laser triggered system was used to collect the experimental data and a MATLAB code was used to elaborate the output data. The test were performed following the BS EN ISO6603-2:2000 standard evaluating the impact behaviour of two different wires configurations: Bottom W configuration was tested with wires on the opposite side of impacted surface, while Top W configuration with copper wires close to loaded area. Samples were compared with a traditional CFRP laminate (Ref) obtained with the same stacking sequence but without any metal reinforcement.

3.2 Sensing feature

Both tests were performed using an Instron Universal Tester (3369) to apply the displacements on Sens Cu and Sens SMA while a 6 ½ digit multimeter (VOM) Agilent 34401A monitored the electrical resistance during the tests. Three-point bending tests were performed on each sample placing them on two supporting pins at a set distance apart while a third loading support was lowered from above at a constant rate of 0.2 mm/min until sample failure. The applied load generates tensile stress in the convex side of the specimen and compression stress in the concave side. Insulating tape (PTFE) was used to avoid any interferences that could affect the resistance measurements. Punch tests were conducted using a spherical tip of hardened-steel and applying the load to an exact point on the sample. The sample was constrained on a hollow support using four G-clamps on its four corners and the punching support was lowered at a constant rate of 0.2 mm/min. Hence, it was possible to partially extend the results taken from the static case (punch test) to the dynamic case (impact load) as reported in literature [44] [45] since in both cases, an external displacement is applied on a single point of the sample.

3.3 Damage detection

To test the feasibility of this approach two different configurations were investigated. For single wire configuration, the test was performed generating heat from each of the different wires within the laminate structure; the current applied in this case was of 3 A. For multiple

excitation of the wires, a multiplex system managed by an Arduino module was designed and manufactured in order to generate heat by applying a current in a sequence on all the wires. Since it is possible to scan with a specific frequency even large samples, by using this approach it is possible to reduce the total amount of power required. In addition, when the system is used together with the strain detection method, only specific portions of the sample (i.e. the critical parts in complex structures) can be scanned diverting more power on smaller areas, thus increasing the resolution of the inspection while keeping the required power to the minimum. In this case, the current applied was of 1.5 A. Since the position of the wires will determine the relative distance between the potential damaged area and the portion of the samples accessible for the thermal analysis, different typologies of hybrid samples were tested and subjected to different damage conditions:

- **SMA/CFRP (Therm-PTFE, LeadingEdge-PTFE and LeadingEdge-SMA):** Therm-PTFE and LeadingEdge-PTFE samples were manufactured with an embedded Polytetrafluoroethylene (PTFE) patch to simulate the presence of a damaged area at a certain depth within the laminate structure. The samples were analysed with both the single wire configuration and the multiplex system. Leading Edge SMA instead was manufactured with no PTFE patch and subjected to a LVI to generate a real internal defect.

- **CU/CFRP (Bottom-W and Top-W):** The copper hybrid samples were manufactured with no patches and subjected to a Low-velocity Impact (LVI) using a weight drop tower in order to generate barely visible impact damage (BVID). The used energies were 20J and 25J. The samples were investigated using only single wire configuration and a comparison between the different damaged areas was reported.

A power supply provided for the continuous electrical current (3 A for single wire configuration and 1.5A for multiplex one) and an electrically cooled Ir camera (CEDIP) was used to collect thermal data with a resolution of 320x240 pixels (weight x height), maximum frame rate of 150 Hz and temperature sensitivity of 30 mK. Digital units (apparent temperature) are the camera units used to evaluate the intensity of the thermal radiation (emissivity) recorded in a certain interval of time. In order to obtain an estimation of the real temperature of the body, can be related to the camera temperature sensitivity [37]. However, since the real temperature measurement can be affected by several conditioning parameters including material thermal properties, environmental conditions and camera focus, all the thermal images are reported using digital units instead of °C in order to present thermal results with the best resolution, free from external conditioning. All measurements are recorded at room temperature (25°C). Because of the presence of the internal heat source, it is possible to use different typologies of thermographic inspection such as Pulsed Thermography (PT), Pulsed Phase Thermography (PPT), Lock-In Thermography (LIT) and Step Heating Thermography (SHT) without the need of additional equipment or specific setup. In this case a SHT method was used in order to detect damaged areas also at deeper locations inside the laminate, and the camera was used to monitor the magnitude of the apparent temperature variation on the sample surface during both cooling and heating processes. A background subtraction was executed on the measurements selecting 100 frame before the heating process and calculating the data average for each images' pixel. The total observation time was 5 s for the single wire configuration and 9 s for the multiplex configuration with 0.01 s of interval for wires switching.

3.4 De-icing feature

A thick layer of ice was built up on sample surface using a freezing spray agent and thermal scanning of 30 s was conducted heating up the wires. Using electricity passing through the wires (0.55 A and 3.04 V), heat can be generated to locally increase the surface temperature of the sample and melt the ice on its surface. In order to increase the temperature of a large area by using a single power supply, to keep the power consumption low and to route the heat only the most sensitive zone of the part (leading edge), the multiplex configuration was chosen. Thermal data were collected using the same camera configuration used for the previous tests. Results were reported at three different time steps (0 s, 15 s and 30 s) to illustrate the effective ice dissolution. All the tests were performed at room temperature (25°C). Mechanical properties detriment is a well-known issue for commercial de-icing systems already used on structural components and mainly depends on two factors: the time of actuation and the temperature intensity. It was demonstrated that when a CFRP component is exposed at temperatures of 100-150°C for 45 min, a detriment of the mechanical properties occurs with a loss of ~6% -14% [46] and that a severe degradation of the material occurs when exposed to a temperature over 180°C [47]. Analysing the typical temperatures involved during the heating of the metal reinforcement and the time of actuation of the heating system, it is possible to identify a range of temperature of 50-80°C [37, 48] for a time of 9-30 s. Consequently, comparing the used temperature and time of activation of the hybrid system with the critical ones, it is clear that the mechanical properties detriment due to heat transfer can be assumed very small and localized around the metal area with no influence on the general properties of the laminate.

4. Results and discussion

4.1 Impact Campaign

The impact campaign was conducted in order to understand the real improvements in terms of mechanical properties when metal wires are embedded within the CFRP during the manufacturing process as additional reinforcement. Although previous results in literature indicated that the best location along the thickness for metal wires is close to the impact surface [19], it is necessary to confirm this on the manufactured H-CFRP in order to understand the best position of the embedded network along the laminate's thickness in order to maximise the efficiency of the non-structural functionalities. In fact, as described in this work, the position of hybrid network through the thickness is important for accurate damage detection and strain sensing functionalities. Based on this consideration, it is important to consider how the metal network location changes affect the impact resistance of the proposed hybrid material. During an impact the hybrid laminate is also loaded in the out-of-plane direction, and the impact energy will absorbed by damage, and plastic deformation of the wires. In this work, a comparison between two different hybrid composite configurations under impact loading is presented. The two tested configurations, as previously reported, are structured in function of the relative position of wires and impacted surface. For thin walled structures, during the impact event, the laminate portion below the neutral plane is subjected to tensile stress while the other part, is interested by compressive one. For brittle materials [49], these tensile stress should be minimised, hence, the array of metal wires has the function of absorbing as much impact energy. Moreover, as illustrated by Bradley [19], the structure failure modes are different in

function of the presence of wires: if the wires are close to impacted area, the sample's stiffness is locally increased and the failure mode is no more by buckling compression, but shear failure is the main cause of composite breakage. Analysing the failure mechanism of the two wires configurations, it is possible to identify two opposite behaviours. When metal arrays are located far from the impacted area (tensile portion of laminate), the impact energy propagates across the sample's thickness, generating, in the compressive zone, moderate damaged zones (buckling compression). However, across the middle plane, the stress typology switches from compression to tension, leading to a different and more dangerous situation. Along the wires, the crack extension is intensified by a two different mechanisms: weak matrix-metal interface (that creates a preferential zone for cracks' nucleation and propagation), and stresses accentuation around discontinuities edges. These mechanisms coupled with the tensile stress (that accelerates the defect propagation), lead to a catastrophic and sudden failure of composite with massive damaged area in the lower part of laminate. On the other hand, when the hybrid component is localised on the compressive zone of laminate (in the proximity of the impacted area), the impact energy generates a damaged area on the portion around the length of wires where no weak zone are present. Dissipating a large amount of energy both to plastically deform the wires and to propagate the cracks, reduced delamination area can be observed. Based on this consideration, the best eligible configuration to increase the mechanical properties of laminate is expected to be the one with wires in the compressive portion of plate, as close as possible to the impacted zone, in order to dissipate as much energy as possible in the less sensitive part of composite [19, 50]. The experimental data confirms the validity of the previous concepts as shown in Figure 2.

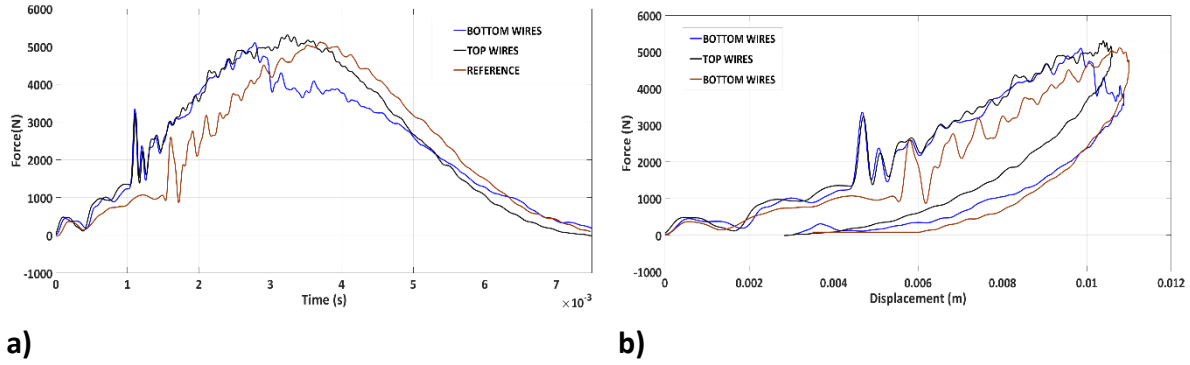

Figure 2-Force-Displacement curve of different wires configurations: a) Time – Force plot and b) Displacmeent-Force plot.

The best behaviour is shown from the Top W configuration, which has wires close to the impacted surface and the maximum contact load recorded during the tests (5281 N). On the contrary, Bottom W shows an evident load drop in the impact curve, suggesting structural collapse in progress inside the sample. Comparing the Top W and Ref (reference), it shows that the Top W has a slightly improved impact behaviour than traditional CFRP at relative maximum displacement value. On the other hand, the hybrid component has a negative effect on Bottom W since the load drop is more pronounced than the reference, indicating a worse structural breakage during the impact event. An improved impact response for the sample with top wires was confirmed by ultrasonic phased array inspections. A 5 MHz Phased Array Transducer with 128 Channels (National Instrument) was used for this purpose. The difference in terms of delaminated area is reported in Figure 3 where amplitude colour map is shown for each plate. The extent of the delaminated area was calculated using an image processing software and the measurements are reported in Table 2. The smallest delaminated area is found in the Top W -4% smaller than the Ref one, while, the Bottom W damaged area is +18%

greater. Absorbed energy and maximum tolerated load are also reported in Table 2 together with delaminated areas extension.

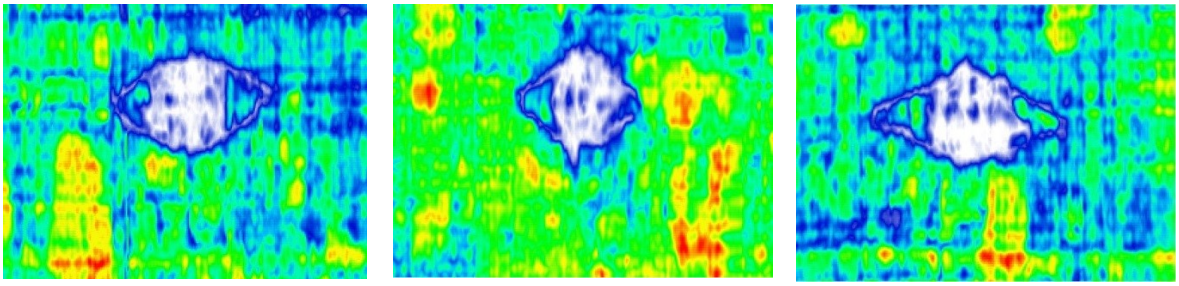

BOTTOM TOP REFERENCE

Figure 3-Ultrasonic Phased Array ultrasonic scan with wires positioned at different locations within the samples thickness and traditional unreinforced laminate.

Table 2-Impact energy absorbed, maximum load, maximum displacement and damaged area for Bottom W, Top W and Ref configurations with statistical variation (3 samples for each configuration).

Samples	Typology	Absorbed Energy [J]	Maximum Load [N]	Maximum Displacement [mm]	Damaged Area [mm^2]
1	Bottom Wires	14.85±1.48	5235±151	7.64±0.43	1128±136
2	Top Wires	14.51±0.23	5281±57	7.53±0.07	884±54
3	Reference	14.46±0.18	5077±151	7.54±0.17	919±24

4.2 Sensing Features

The hybrid phase can be also exploited as strain sensor to detect the position and the magnitude of the external stimulus, monitoring the change of its electrical resistance. Two typologies of tests were conducted: 1) three-point bending to investigate the correlation between resistance variation and displacement when a distributed load is applied and 2) punch test to test the reliability of the method to detect impact-like events.

In order to evaluate the electrical resistance variation avoiding differences given by the wires length and measurement fluctuations, a normalised electrical resistance $\bar{R}$ is calculated using as reference the electrical resistance of the wire when no displacement is applied. According to the equation (1), the normalised resistance is calculated:

$$\bar{R} = \frac{R_n - R_0}{R_0} s \quad (1)$$

Where: R_n: measured resistance [Ω] and R_0:reference resistance [Ω].

Equation (2) is used to calculate the electrical resistance of a metal wire:

$$R = \rho \frac{L}{S} \tag{2}$$

where, ρ: the resistivity of the material [Ω·m], L:length of the wire [m] and S is cross section of the wire assumed constant [m^2].

Assuming that a uniform load is applied along the midspan of the sample, it is possible to consider each laminate-wire system as a 1D beam under bending loading (Figure 4) and the beam theory can be applied. It is assumed that the plate and the wires are well-bonded and have no relative displacement when a load is applied uniformly along the span of the plate. Consequently, the flexural solicitation of wire and laminate has the same value.

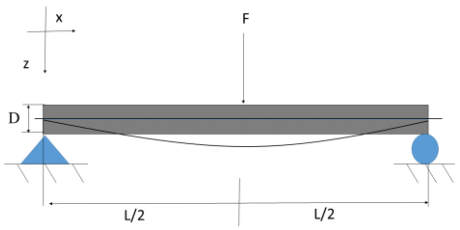

Figure 4-Scheme of 1D beam simply-supported

In order to calculate the deflection of the beam, the Euler -Bernoulli beam theory can be used:

$$\frac{d^2}{dx^2}\left(EI\frac{d^2w(x)}{dx^2}\right) = q(x) \tag{3}$$

where, w (x): deflection of the beam in the z direction at some positions x [m]; q: applied force for unit of length [N]; E: Elastic modulus [GPa]; I: Second moment of area [m^4]. In order to obtain the maximum deflection in the centre of the beam, the hypothesis of small deformations, linear elasticity and normal neutral surface are assumed. Solving the equation for this supported beam configuration, the deflection of the beam, the slope ϑ(x) and the bending moment M(x) in function of the x-position along the beam can be written using the Macaulay's notation [51]:

$$M(x) = \frac{1}{EI}\left(\frac{F}{2}\langle x\rangle^1 - \frac{F}{2}\langle x - \frac{L_0}{2}\rangle^2\right) \tag{4}$$

$$\vartheta(x) = \int M dx = \frac{1}{EI}\left(\frac{F}{4}\langle x\rangle^2 - \frac{F}{2}\langle x - \frac{L_0}{2}\rangle^2 - \frac{F{L_0}^2}{16}\langle x\rangle^0\right) \tag{5}$$

$$w(x) = \int\int M(x)dx = \frac{1}{EI}\left(\frac{F}{12}\langle x\rangle^3 - \frac{F}{6}\langle x - \frac{L_0}{2}\rangle^3 - \frac{F{L_0}^2}{16}\langle x\rangle^1\right) \tag{6}$$

where x is the position along the x-axis [m]; F the force applied on the sample [N]; and $L_0$the initial length of the beam [m]. The subscript c is used to reference the laminate parameters while with the subscript w, the wire's ones. The maximum deflection evaluated in the centre of the beam at $L_0/2$ is:

$$w_{max} = \frac{F{L_0}^3}{48E_cI_c}. \tag{7}$$

This value represents the flexure extension applied by the test machine on the sample.

The relation between bending moment and longitudinal stress is expressed using the equation:

$$\frac{M(x)}{I_c} = \frac{\sigma(x)}{z} \tag{8}$$

where z is the distance in respect to the neutral plane of laminate along the z-direction that corresponds to the wire location [m] and $\sigma(x)$ is the longitudinal stress [Pa] defined using the elastic constitutive law ($\sigma(x)=E\varepsilon(x)$). Since the displacement of wire and laminate is the same under bending conditions, the longitudinal strain of the laminate at the z-distance from neutral plane corresponds to the longitudinal strain of the wire placed at same distance from the neutral plane. Moreover, considering the relative position between wires and middle plane of the laminate (Figure 5), it is possible to observe that the wire is very close the outer surface of the sample, therefore the term z in the equation above can be assumed as equal to half the thickness of the sample (D/2).

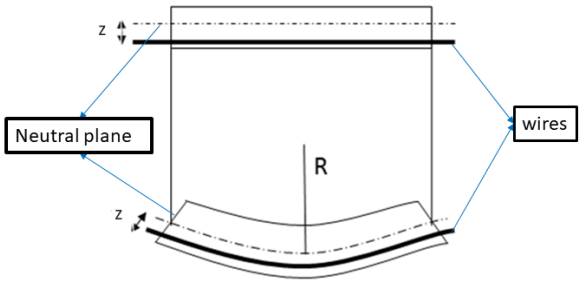

Figure 5 -Configuration of wires within the laminate

According to the equation 8, the longitudinal strain $\varepsilon(x)$ can be written as:

$$\varepsilon(x) = \frac{z}{EI}M(x) \tag{9}$$

In order to estimate the longitudinal strain ε_c at positon z along half of the laminate length (symmetrical view), an integral view is used considering:

$$\varepsilon_c = \int_0^{\frac{L_0}{2}} \varepsilon(x)\,dx = \frac{z}{E_cI_c}\int_0^{\frac{L_0}{2}} M(x)dx. \tag{10}$$

Using equation (6) for the bending moment equation and considering the first portion of beam, the total longitudinal strain is calculated:

$$\varepsilon_c = \frac{{L_0}^2 z}{16 E_c I_c} F. \tag{11}$$

Under the aforementioned hypothesis, the bending moment applied on the laminate (M_c) is equal to the bending moment applied on the wire (M_w):

$$M_c = M_w \tag{12}$$

Using equation (9) in (12), it is possible to calculate the longitudinal strain applied on the wire (assumed as a cylinder) during bending:

$$\varepsilon_w = \alpha \varepsilon_c \tag{13}$$

$$\alpha = E_c I_c / E_w I_w \tag{14}$$

It is important to notice that the differences in terms of mechanical and geometrical properties between composite and wire are considered into the coefficient α. Due to the two different strains of composite and wire, shear stress is generated along the resin interface between the two components. This interface is assumed totally elastic under the hypothesis of perfect bonding.

By considering the expression of ε for the wire's strain calculation:

$$\varepsilon_w = \frac{L - L_0}{L_0} \tag{15}$$

It is possible to write the final length L using (11) and (12) as:

$$L = \alpha \frac{{L_0}^3 z}{16 E_c I_c} F + L_0 \tag{16}$$

This equation represents the length in function of the applied load.

From (2) and (13):

$$R = \frac{\rho}{S}\left(\alpha \frac{{L_0}^3 z}{16 E_c I_c} F + L_0\right) \rightarrow R = \Delta R + R_0. \tag{14}$$

Based on equation (14), it appears clear that by analytically evaluating the resistance variation of the embedded wires, it is possible to detect the intensity of an applied flexure load on the sample. It is possible to notice the linear trend of the equation with a slope equal to the first term of the expression (ΔR) and with second term as intercept (R_0). The intercept represents the value of the resistance for the unloaded wire, while the slope represents the variation in resistance generated by the flexure loading.

It is possible to rewrite equation (14) in function of the flexure extension, by using the deflection definition equation (6):

$$R = \frac{\rho}{S}(3z\alpha w_{max} + L_0). \quad (15)$$

This equation allows to calculate the theoretical behaviour of the resistance in function of the flexure extension applied during the three-point test. In this case, the first term is the slope of the line while the second remains the intercept.

In order to validate the analytical model illustrated above, samples were tested on both sides in order to generate respectively elongation and compression on the wire under test. The two behaviours have to follow the equation (16) where the z-value is positive in the positive direction of z-axis if the wires are in the lower part of the composite, while negative when the wires are in the upper part of the laminate. During the test campaign, Sens-Cu and Sens-SMA samples were tested, however only for Sens-SMA samples it was possible to correlate the resistance variation with the applied displacement. Sens-Cu samples, in fact, showed no correlation due to the low resistivity of copper ($1.68 \cdot 10^{-8}$ Ω·m) which generated a very small resistance variation. The multimeter used was characterised by limited number of digits and the measured resistance was below the instrument sensitivity. Consequently, the resistance variation recorded during the test was not the real one but the result of a truncation error that affected the measurement. On the other hand, Sens SMA showed good correlation between the two parameters since the SMA resistivity ($1.08 \cdot 10^{-6}$ Ω·m) is considerably higher than copper one leading to higher resistance variation. The experimental results for three-point bending test are shown in the figures below. **Error! Reference source not found.**.a represents the mechanical data collected during the flexural test where the flexural load follows a linear trend with the flexural extension, in accordance with [52]. In **Error! Reference source not found.**.b, the theoretical behaviour of the resistance variation and the experimental curves show a comparable linear trend for low values of flexure extension that tends to slightly diverge for higher values of the flexural extension since the hypothesis of small displacement is not valid due to a large deformation of the wires (26%) that can lead to a mismatch with the theoretical prevision for high values of flexure extension. From **Error! Reference source not found.**.b and the **Error! Reference source not found.**.c, the resistance variation with increasing flexural extension follows a linear trend hence, it is possible to monitor the strain distribution by measuring the behaviour of electrical resistance. In order to verify the same trend of resistance variation when the wires are compressed, a second test was performed. In this case, the sample was set in the test machine with the wires facing the loading support in order to apply compressive stress on the SMA wires (Figure 6.c). By analysing the behaviour of the same wire in both compression and tension, it is possible to estimate the trend of the two configurations and observe the same modulus for each experimental point as shown in **Error! Reference source not found.**.d.

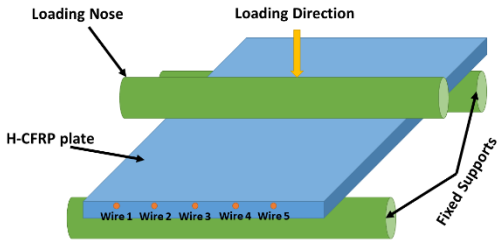

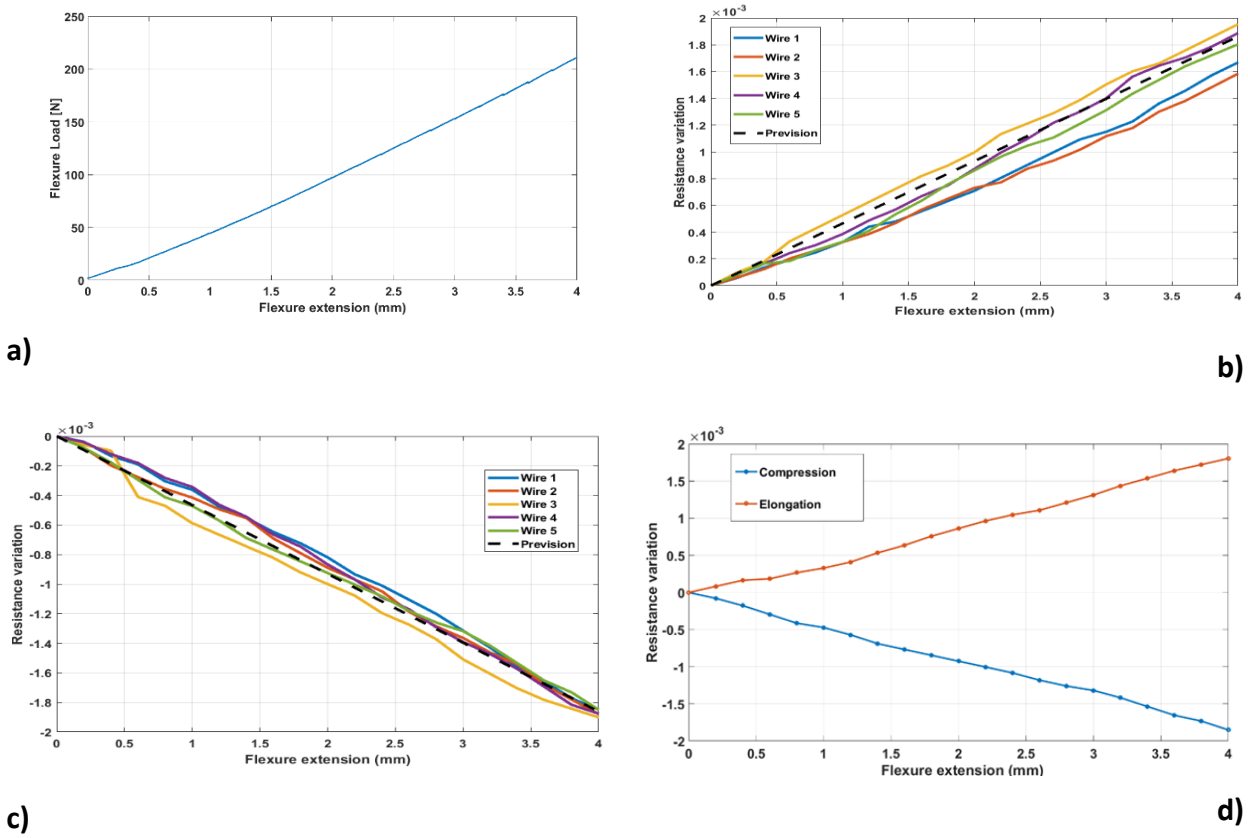

Figure 6-Experimental data for three-point bending test: a) Flexure Load vs. Flexure extension curve. b) Electrical resistance variation curves with stretched wires. c) Electrical resistance variation curves with compressed wires. The theoretical prevision is reported.

Since, the good correlation between theoretical and experimental data confirmed the correlation between the applied load and the variation of the electrical resistance of the wires, a punch test was performed to investigate the possibility to detect the exact position of an impact event applying a concentrated deformation in a single point rather than over the entire width of the sample. This model was realised considering a static case where SOLID45 (eight nodes and orthotropic material properties) elements were used. The displacement of 4 mm (maximum applied displacement measured during the tests) was applied at the centre of the top surface in correspondence with Wire 3. The sample was constrained on its four corners, fixing all the degrees of freedom. The plate's dimensions were 150 mm x100 mm x1.3 mm.

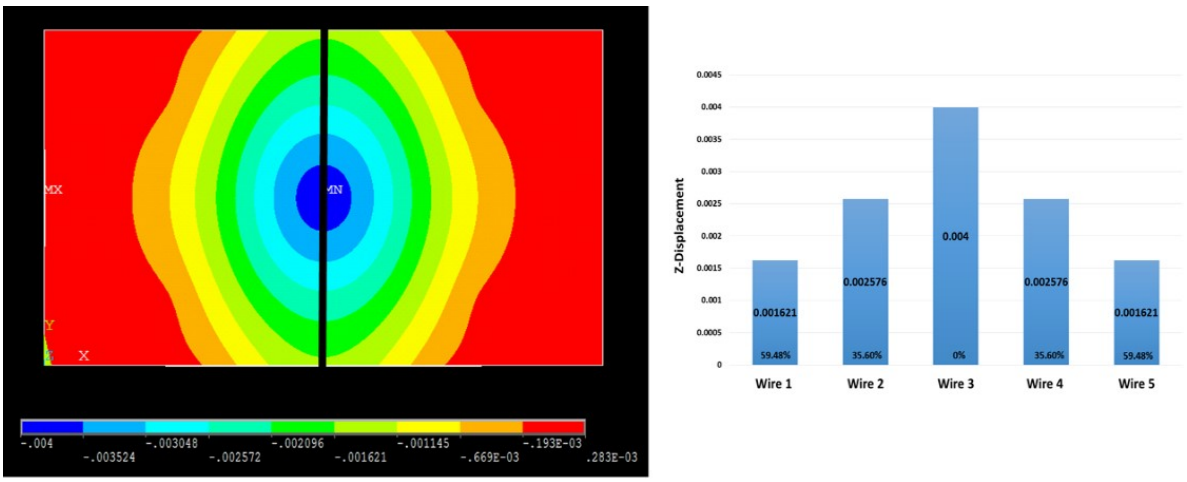

Figure 7-FEM model of the CFRP sample (frontal view). Z -displacement is shown using the colour-map to estimate the magnitude. The maximum deflection values are indicated by the black line. Displacement values are evaluated for each wire considering their maximum deflection and percentage reduction respect to the experimental displacement applied.

From Figure 7, the maximum displacement corresponds to the location where the tip applies the load and the external rounded zones are progressively less interested by the deformation. Along the black line, the maximum deflection can be linked to the previous test where the maximum deflection was applied by the moving pin. Considering that on that line, the conditions of maximum deflection, mandatory for the theoretical model, are still valid, it is possible to extend the theoretical model developed for the three-point bending test to the punch test. In Figure 7, displacement and wires position are reported and qualitatively, it is possible to determine the magnitude of the resistance variation for each wire. As mentioned previously, the Wire 3 location is where the maximum displacement is observed and where z-displacement is equal to the punching deformation. Wire 2 and Wire 4, symmetric respect to Wire 3, are characterized by a lower elongation since, the z-displacement magnitude is reduced by 35.6% in the area surrounding the punch location Wire 1 and Wire 5 instead, are located in an area on which the z-displacement is reduced by 59.47% than the central one. Consequently, the values of resistance variation measured on the external wires will be less relevant than the ones measured for the internal wires. These results show that by monitoring the resistance variation of the embedded wires network it is possible to localise the presence of an impact event in real time on the surface of the sample. In Figure 8.a,the flexure load follows an exponential trend with the flexure extension which it is congruent with the other experimental data in literature for compressive test on CFRP [53]. In addition, in Figure8.a, the resistance variation in function of the flexure displacement is illustrated, reporting a different response of the metal wires when the flexural displacement is applied on the centre of the sample. The greater resistance variation is shown by the Wire 3 trend while the other wires exhibit lower values. The displacement is applied directly on the Wire 3 position which reports a behaviour similar with what observed during the three-point bending test (**Error! Reference source not found.**). Indeed, as shown from the FEM model, the maximum deflection is located in that point and consequently, the theoretical model used for the correlation of the three-point bending tests can be extended to associate the experimental data of Wire 3 during the punch tests. On the contrary, the other wires respond with a very low fluctuation of resistance because their displacement values are lower than the central wire ones, hence the theoretical model is not applicable in these locations. The comparison between the experimental data collected of Wire 3 and the theoretical model for three point bending test matches for low-middle values of displacement while for higher values there is a slight mismatch due to the small displacement assumption.

However, the experimental data proved a good correlation between displacement and resistance variation for the Wire 3 and the ability to identify the presence of an applied load caused by an impact event.

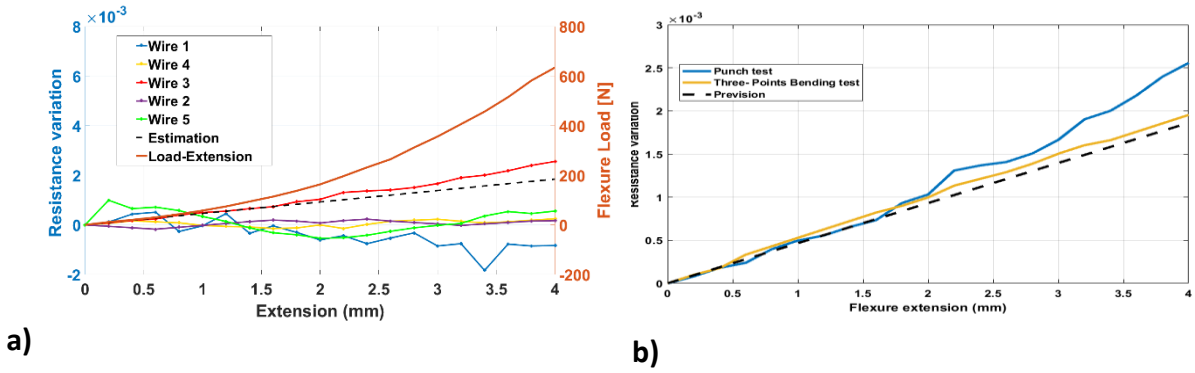

Figure 8-Experimental data for punch test: a) Flexure Load vs. Flexure extension curve and Electrical resistance variation curves with theoretical estimation for Wire 3; b) Comparison between Wire 3 results for the different tests. The prevision is reported.

4.3 Damage Detection

Exploiting the thermo-resistivity of embedded metal wires, it is possible to scan composite structures and identify the delaminated areas. By applying an electrical current to the wires a thermal wave via Joule effect are generated and propagates towards the surface and monitored using an Ir thermal camera.

- ***SMA/CFRP with PTFE patch***

Unlike metals whose thermal properties are isotropic, for composite materials along the fibre direction, the thermal conductibility is higher than in the transverse one because the resin reduces the thermal conductibility. Hence, the heat diffuses not uniformly along the principal directions of the material. This allows identifying a zone where thermal diffusivity is different from the rest of the part, as in the case of a delaminated area. The rate at which this wave propagates in the sample for a given current generated at a given depth depends on physical properties of the entire sample (as thermal conductivity) and it is strongly affected by any discontinuities within the laminate thickness. Hence, the presence of an internal damage would interact with the wave propagating from the embedded wire towards the top surface, leading to a localised variation of the apparent temperature in an area on the surface perpendicular to the damaged point.

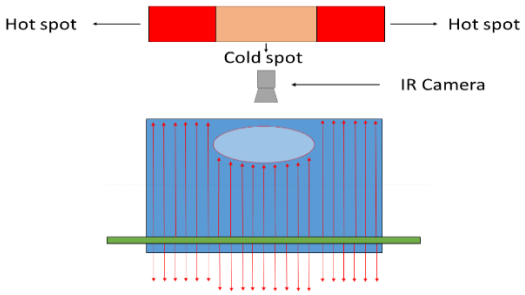

Figure 9 – Layout heatwave propagation inside hybrid CFRP composite interacting with a delaminated zone (PTFE patch), far from the delaminated area.

This is illustrated in Figure 9 where the camera is able to identify hot spot zones that correspond to areas in which the heat is not influenced by the internal discontinuity and cold spot zones where instead the heat is unable to propagate due to the presence of structural discontinuities (PTFE patch). Therm-PTFE was analysed by placing the Ir camera in front of the sample, facing the PTFE patch. Figure 10 shows the results captured from two different points laying on different portions on the same wire. In particular, the orange curve corresponds to an undamaged area, while the blue curve represents the variation of the superficial apparent temperature in a spot placed perpendicularly to the PTFE patch. The graphs show a thermal wave propagating in the sample's thickness towards the top surface, leading to an increase in the apparent temperature. In facts, the heatwave is slowed down due to a lower thermal conductibility of discontinuity and, due to the non-homogenous thermal properties of CFRP, the heatwave is unable to go around the damaged area, spread in the transverse direction and mask the delaminated area. The sign of the apparent temperature variation (whether positive or negative) depends on the relative positions of the damage, the heat source and the Ir Camera.

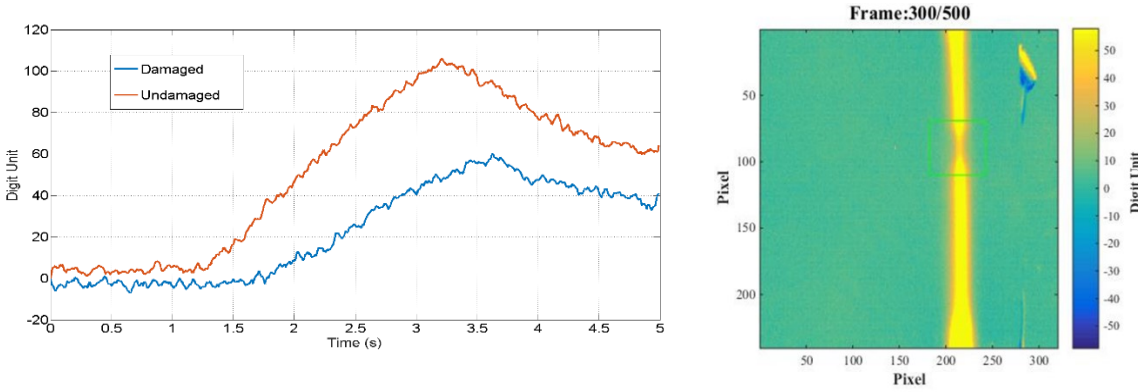

Figure 10 -Images acquired during the test after the background subtraction operation for Therm SMA, together with the curves recorded from two areas corresponding to a damaged and undamaged spots on the sample's surface.

The presence of the discontinuity affects both the amplitude and the slope of the curve relative to the damaged area allowing a rapid localisation of the internal damage from the heating and cooling portions of the curve. One of the drawbacks of the single-wire configuration is the necessity to connect each wire to a different power source to generate a heat gradient large enough to scan the entire surface of the part under examination. This requires a large consumption of power since each wire needs to be fed separately. In addition, the connections and electric circuits on each wire can locally affect the generated gradient in different areas of the samples, leading to reading uncertainties and detection issues (i.e. false positives). To overcome this limitation, a multiplex system was designed and built able to scan the sample by automatically switching between the different wires, synchronising the length of the excitation

for each wire and regulating the current; this reduces the power requirements since the multiplex system requires only a single power supply channel to be connected. The curves captured with the multiplex system are presented in Figure 11 and show a trend similar to the one observed in the single wire configuration. In this case, however, due to the scanning system, the heating is limited at a defined time interval. The interval between the excitation of each wire plays a fundamental role in the output of the results. In particular, it was found that when the interval time τ is too small (in the interval between 5-500 ms) the generated heat wave at first is not able to reach the surface and it slowly diffuses into the laminate bulk. This slow propagation is able to "mask" the presence of the internal damaged area since the heat front has enough time to go around the PTFE patch and reach the top surface. For this reason the scanning time was chosen with an interval τ of 1s.

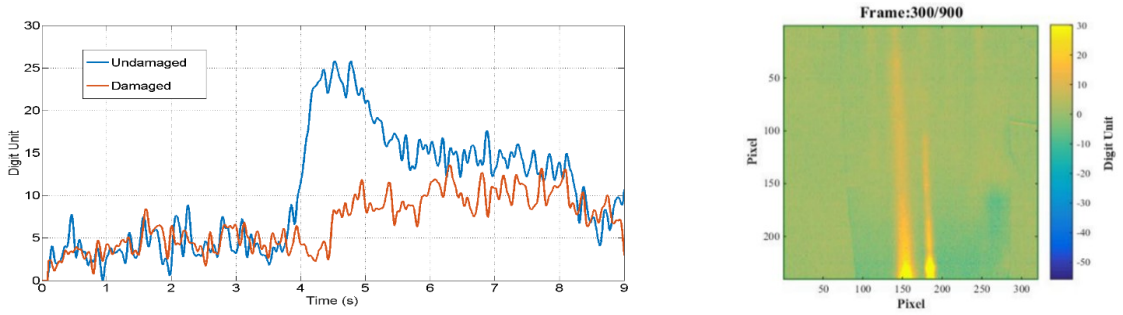

Figure 11 -Apparent temperature variation and thermogram captured for Therm SMA in the multiplex configuration

Two monitoring configurations were tested: Configuration 1 shows wires and camera placed on the same side (the heat crosses only few layer before being recorded by Ir Camera) while Configuration 2 has wires and camera located on the opposite side (the heat crosses the entire sample thickness before being recorded by Ir Camera).

- ***Bottom W: Configuration 1***

Bottom W samples (impacted on the surface far from wires) were analysed by placing the infrared camera on the opposite side to the impact surface using and energy 20J and 25J. The relative position of the wires, impact surface and camera is illustrated in Figure 12:

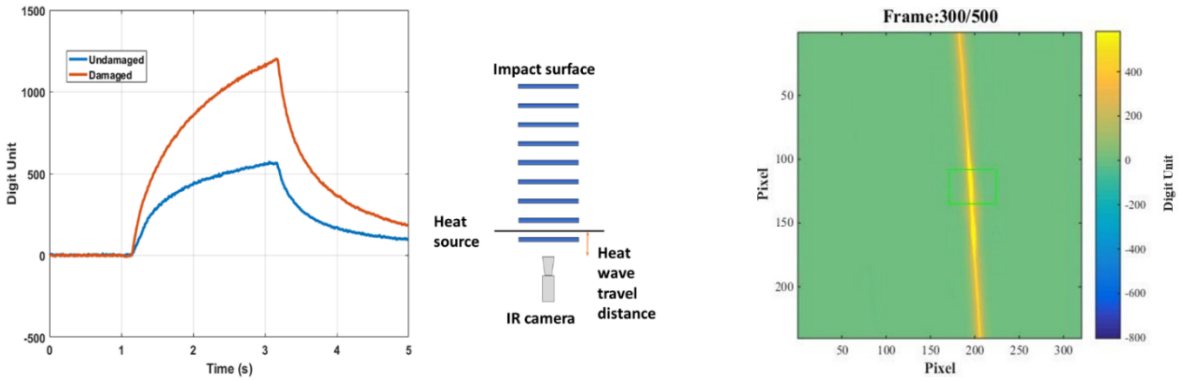

Figure 12 -Thermogram and thermal behaviour after background subtraction for Bottom W (configuration 1 -20J) with relative position of wires, heat source, Ir camera and impacted area.

It shows the variation of the apparent temperature on two spots selected along the same wire: the blue curve represents an undamaged area, while the orange curve is the surface spot correspondent to the 20 J impact point. The colours-scaled image represents the location of the impact damage.

The results show an increase in the apparent temperature change in the damaged area, unlike the previous case. This can be explained by the fact that the delamination caused by the impact is located mostly above the wires (see Figure 13.a), consequently, when the wire is heated, the heatwave cannot propagate through the delamination and heat builds in the opposite direction towards the surface monitored with the Ir camera. As a consequence, the damaged zone shows an increased apparent temperature variation in respect with the undamaged areas.

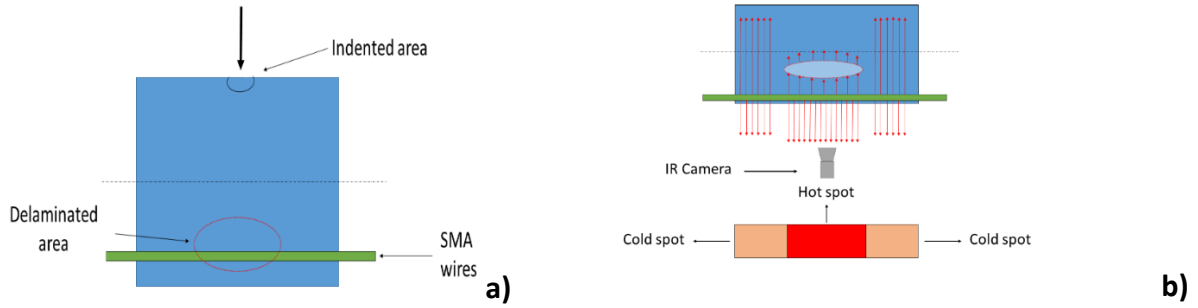

Figure 13 –Bottom W layout after LVI event: a) Relative positions of wires, delamination, impacted area and camera; b) heatwave propagation (red arrows) and heat distribution scheme inside laminate interacting with the delaminated area near the wires. The camera was located close to the wires.

As shown in Figure 13.b, the heatwave is unable to propagate through the delamination due to different thermal properties and, consequently, temperature heat increases in the area free from structural discontinuity that is closer to the camera position. In other zones, the heat can flow without accumulation since no discontinuity is found. The camera, close to the wire position identifies a hot zone where the heat is accumulated (delaminated area) and several cold zones where the heat is free to propagate. Thermal results for Bottom W impacted with 25 J, are reported in Figure 14.

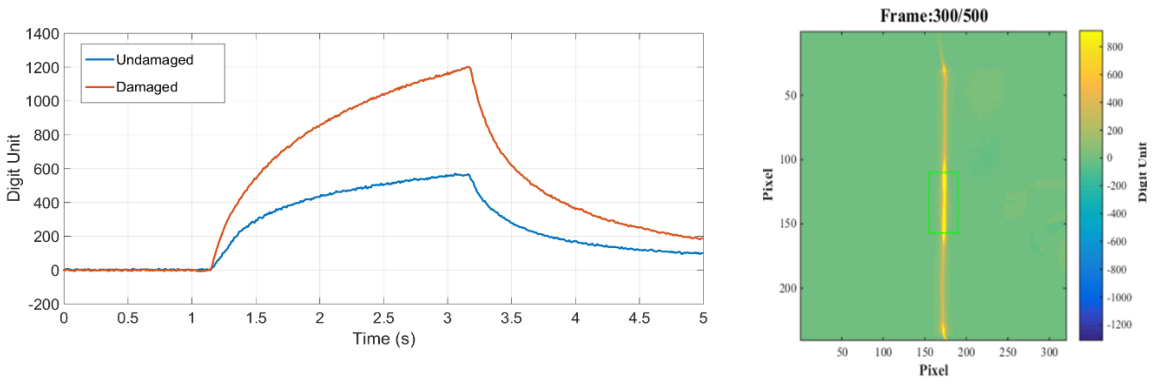

Figure 14 -Thermal behaviour and thermography after background subtraction for Bottom W (Configuration 1-25J)

Impact data at 25 J is comparable to 20J, showing an increase in the apparent temperature variation on the damaged area. To investigate the effect of the impact energy on the thermal response of the two impacted samples, the contrast was calculated with a linear subtraction between the damaged curve and the undamaged curve signals for each set of data using Equation (19).

$$C_{A_i} = \left\| A_{und_i} - A_{dam_i} \right\| \tag{19}$$

Where A_{undi} represent the signal recorded for an undamaged part on the *i*th wire, while A_{dami} is the signal recorder for a damaged point on the same *i*th wire. Figure 15.a shows that the difference between the two signals affects both the portions of the curves (heating and cooling).

The contrast curve of 20J sample is characterised by a lower amplitude in the first heating portion than 25J one, and by an opposite behaviour in the cooling portion. The curve maximum point is higher for the 20 J Bottom W, even though the two peaks are not correspondent due to different turning off times. To quantify the difference between the curves, the maximum peaks difference was calculated for the undamaged curves and the damaged ones using the formula below:

$$\Delta_{peaks} = max_{S7} - max_{S1} \quad (20)$$

Where:
max_{S7} is the Maximum digit unit value of 25 J Bottom W;
max_{S1} is the Maximum digit unit value of Sample 20J Bottom W contrast.

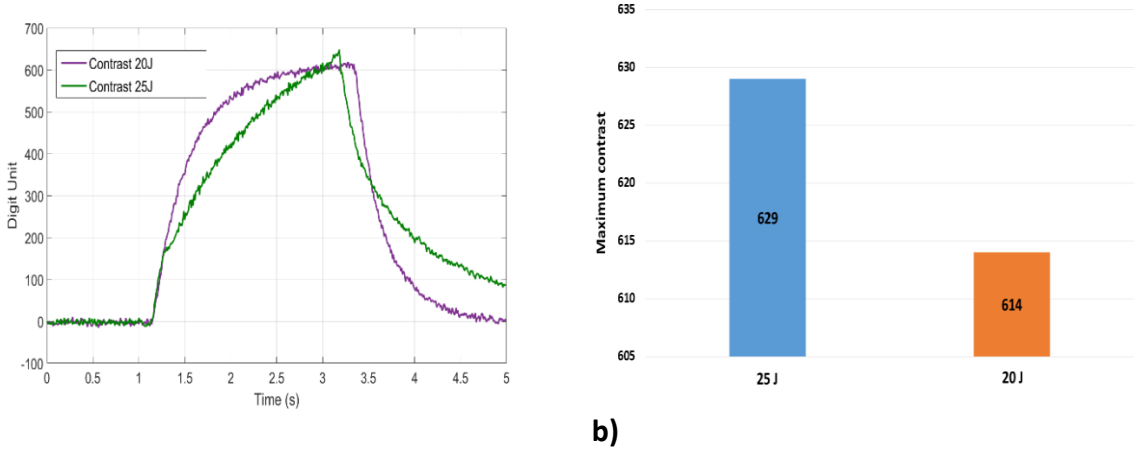

Figure 15– Thermal contrast analysis for Configuration 1: a) Comparison between 25J and 20J Bottom W curves and b) comparison between maximum peaks differences of damaged and undamaged curves of 25J and 20J Bottom W.

As shown in Figure 15.b, results clearly indicate the higher amplitude value of 25 J Bottom W in respect with 20J one. As illustrated previously, this difference in the contrast amplitude can be attributed to the effect of the higher extension of the delamination zone for the 25J impacted sample. A larger delaminated area (as a results of an impact at a higher energy level) affects the propagation of the heat wave in a way which is proportional with the energy level. These results show that there is a correlation between impact energy and amplitude of the contrast signal and can be used to evaluate the severity of the damaged area.

Bottom W: Configuration 2

For Configuration 2, data were collected on the same samples by placing the camera on the same face where the impact occurred (Figure 16.a).
Figure 16.b shows how the heatwave generated from the wire propagates towards the thermal camera. The temperature is slowed down by the delamination while in the other areas, it is free to spread out. The camera, located far from the heat generation wires, records a higher amplitude (hot spot) in the zone where the heat is free to propagate while where the delamination is present, consequently, the amplitude results to be lower, differently from the previous test.

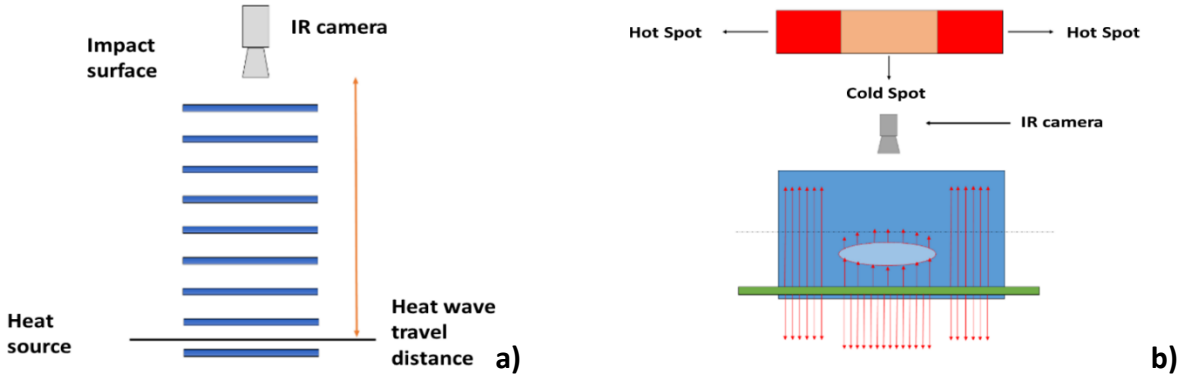

Figure 16-Layout of thermography set-up for Bottom W (Configuration 2): a) Relative position of Ir-Camera, heat source and impact location; b) heatwave propagation and heat distribution scheme inside laminate interacting with the delaminated area near the wires. The camera is located far from wires.

The relative difference between the readings collected from the damaged and undamaged areas (20J) is clear allowing identification of the presence of the damage in correspondence with the impact location as shown in **Error! Reference source not found.**.

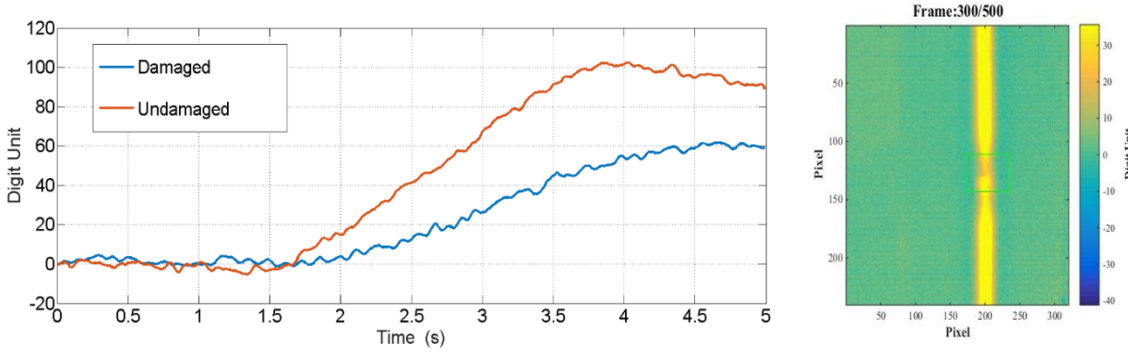

Figure 17-Thermal behaviour and thermography after background subtraction for Bottom W (Configuration 2-20J).

The presence of the impact damage but also the indentation was clearly identified. The compression of composite layers in correspondence of the contact point between penetrator tip and sample surface facilitates the diffusion of heatwave through the laminate that leads to an increase of apparent temperature in that area.

Figure 18 shows the results captured from 25J Bottom W. The image shows clearly where the damage is located as the thermogram shows different amplitude values between the undamaged and damaged zones to indicate the presence of a damaged area. Several bright spots in the central portion of the sample show the zone where the impact took place (indentation), while darker zones indicate the delaminated areas. Comparing thermograms at different level of energy (20J and 25J), it is possible to observe that on the top surface the cold area of 25J sample is larger than 20J one suggesting a more extended internal delamination generated by the higher impact energy applied. As reported for Configuration 1, the comparison between 20J and 25J Bottom W was investigated by a contrast analysis between damaged and undamaged areas.

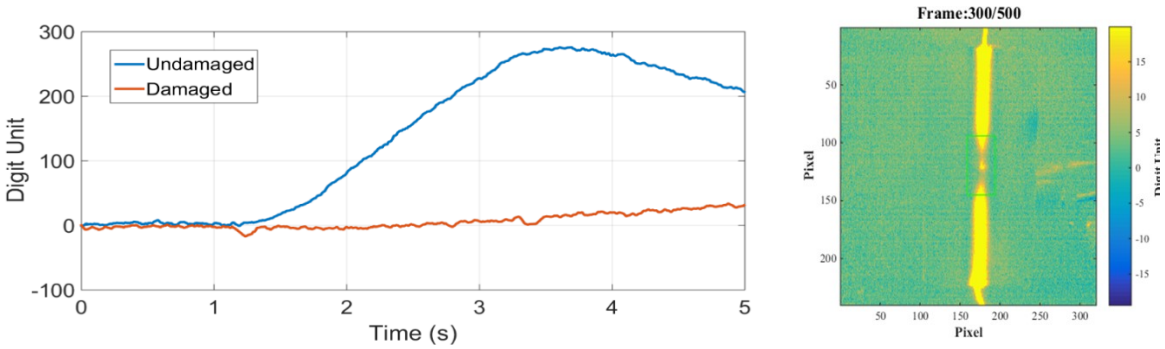

Figure 18-Thermal behaviour and thermography after background subtraction for Bottom W (Configuration 2-25J)

Figure 19.a shows that the difference between the two impact events is even more evident in this case than in the results obtained from Configuration 1. In particular, the contrast signals for the 25J appear to influence both heating and cooling portions of the signals, indicating a more extended internal damage. To quantify this difference, maximum peaks difference is done following the same approach of Configuration 1. Figure 19.b clearly indicates that 25J sample shows a higher amplitude value than 20J sample. As illustrated previously (see Figure 15) also in this case, the delamination zone is more extended in 25J Bottom W because of the higher impact energy. This case is similar to Configuration 1 results.

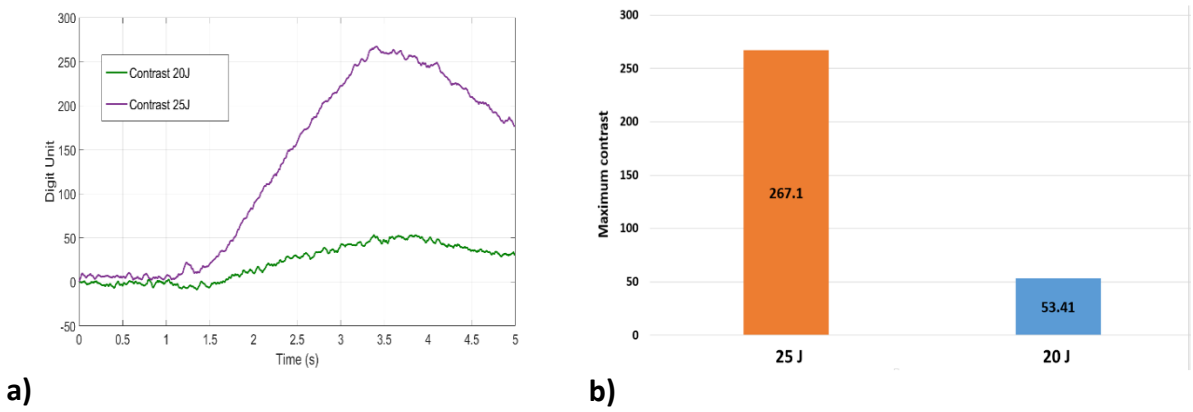

Figure 19-Thermal contrast analysis for Configuration 2: a) Comparison between 25J and 20J Bottom W curves and b) comparison between maximum peaks differences of damaged and undamaged curves of 25J and 20J Bottom W.

- ***Top W: Configuration 2***

It is important to notice that Top W samples were tested by setting up the camera using Configuration 2, since this potentially is a situation more critical than Configuration 1. Since damaged area, wires and impacted area are far from the observation point, the heatwave may spread out without showing the presence of a defected area. In the case of Configuration 1 instead, the situation is similar to the Configuration 1 of Bottom W where the camera is located in proximity of the wires position, impacted area and damaged area that allow to detect easily the discontinuity inside the laminate's body.

Top W samples (impacted on the surface close to wires) were analysed by placing the infrared camera on side opposite to the impact location and using energies of 20J and 25J.
The results collected from Top W impacted at 20J are reported:

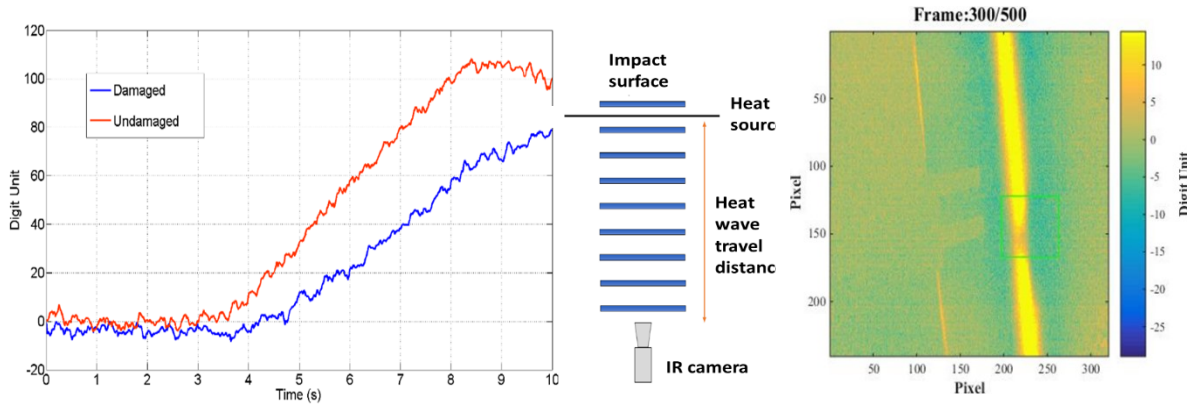

Figure 20-Thermogram and thermal behaviour after background subtraction for Top W (configuration 2 -20J) with relative position of wires, heat source, Ir camera and impacted area.

Analysing the colour map, the delamination does not cross entirely the area correspondent with the embedded wire but seems more concentrated on the right side of the image. This effect is explained with the position of the wire along the xy plane of the laminate. While in the previous case the wire chosen for the analysis was the one passing directly through the middle of the sample, in this case the wire used as heat source was placed on the side of the sample. Considering that the sample was impacted in the centre, it is expected that the damaged areas are more concentrated around the central portion of the sample rather than the sides, which were held in the sample's holder during the impact test. It is important to notice that even though the heat source is not directly positioned on the delamination, the superficial apparent temperature gradient not only allows the identification the damaged areas but it also gives information regarding the correct position and extent of the delamination along the xy plane of the laminate. The schematic layout is reported in Figure 21.

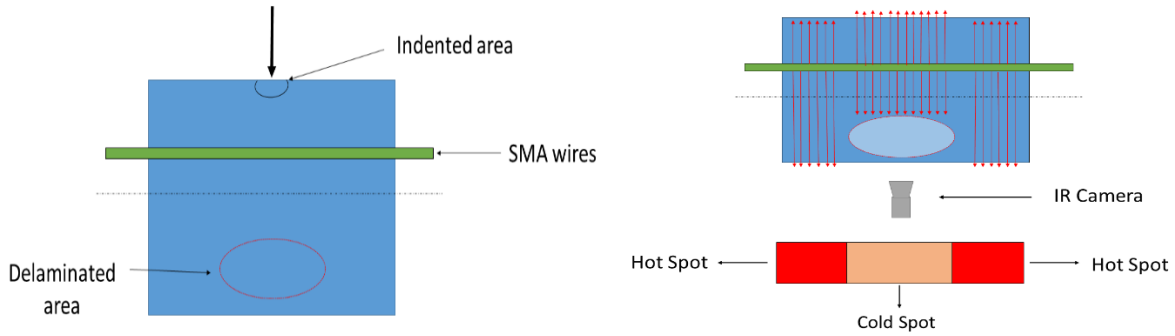

Figure 21-Top W layout after LVI event: a) relative position of wires, delamination, impacted area and camera position; b) heatwave propagation (red arrows) and heat distribution scheme inside laminate interacting with the delaminated area far from the wires. The camera is located far from wires.

Data recorded for 25 J Top W is illustrated in Figure 22 identifying damaged and undamaged areas. In this case, the delamination is far from the wires and the camera is located near to the discontinuity. The heatwave spreads out in the sample but, it slows down (cold spot) near the delamination, while, far from that zone, it is free to flows outside to be recorded from the camera (hot spot).

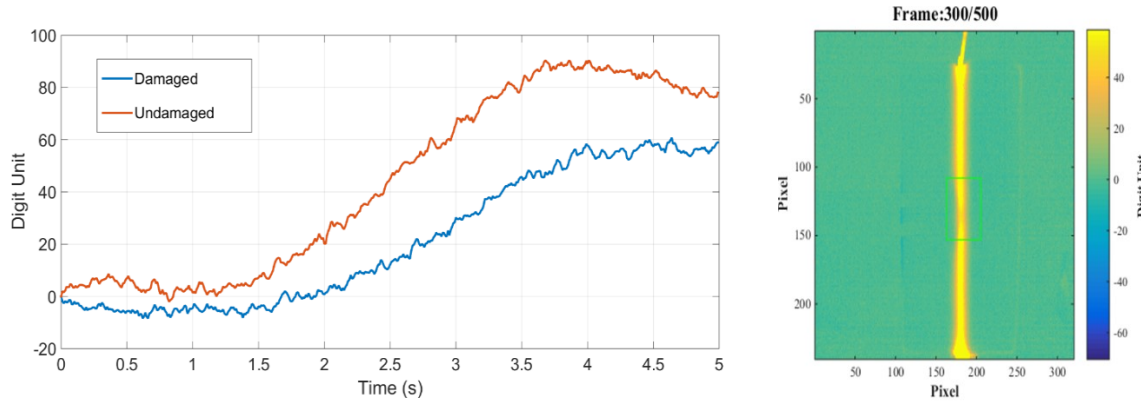

Figure 22-Thermal behaviour and thermography after background subtraction for Top W (configuration 2-25J)

The damage in the 25 J appears less evident than 20J one, but it is visible in the thermogram after the background subtraction. The thermogram shows a marked difference from the hot (undamaged areas) and cold (damaged areas) spots. To determine the entity of the difference in the damage detection, the comparison between contrast and the maximum peaks difference were calculated. From Figure 23, the contrast results similar between the two samples and it is not possible to estimate the biggest damage, even though different impact energy were used, 25J and 20J.

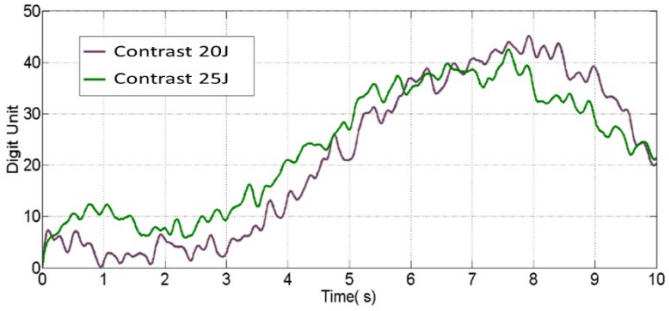

Figure 23-Thermal contrast comparison between 20J and 25J Top W (configuration 2).

This irregularity is caused by the rough thermal data in which, the data fluctuation influences the correct data trend.

- **SMA/CFRP Leading Edge with PTFE**

A Leading Edge-PTFE sample was analysed to evaluate the damaged zone in a complex structure obtaining the same quality and resolution of the analyses on plate-like structures. The PTFE patch was designed using an asymmetrical shape to confirm the validity of the technique even with complex geometry damage. Ir Camera, PTFE patch size and position, and heatwave propagation are reported in Figure 24.

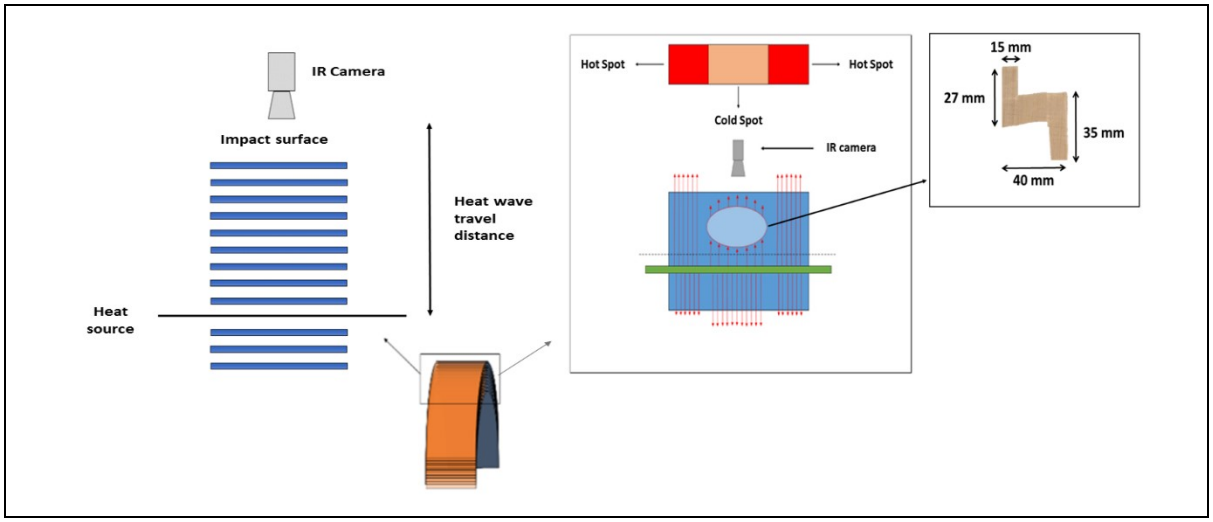

Figure 24-Leading edge PTFE layout and heatwave propagation inside hybrid CFRP composite interacting with a delaminated zone (PTFE patch geometry)

In order to test the effectiveness of the thermography, multiplex configuration was performed. The thermal data recorded by the thermal camera are reported in Figure 25.

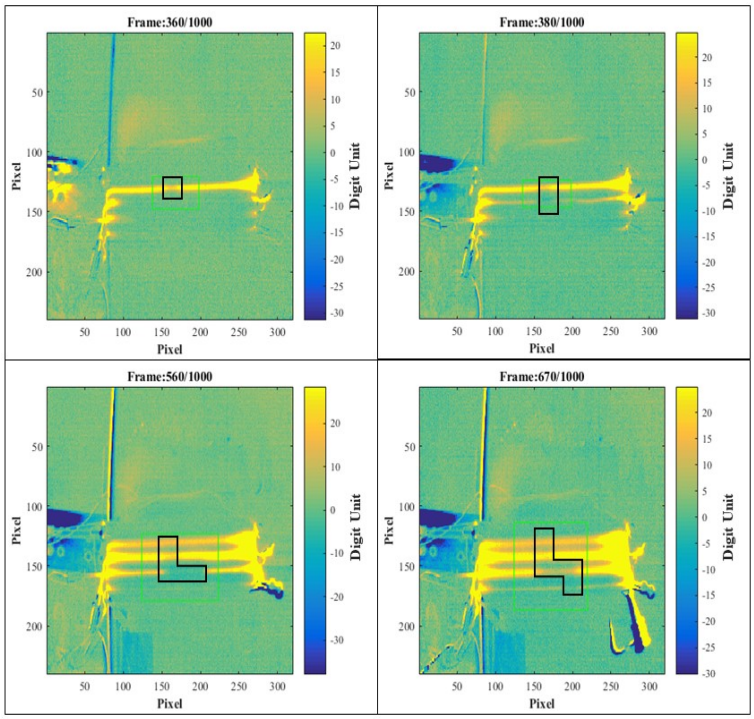

Figure 25 -Thermal images evaluated after the background subtraction procedure for Leading Edge PTFE (multiplex configuration).

It is clear that the heatwave is unable to flow uniformly in the sample because of the thermal properties differences between damaged areas (PTFE patch) and CFRP and, consequently, the generation of hot spots (undamaged CFRP) and cold spots (damaged area) occurs. This behaviour is shown between different wires and it is congruent with a typical heating-cooling curve. Analysing the images it is possible to localise different damaged areas with a similar extent for the wires 2, 3 and 5 where it is evident a small discontinuity along the wire path from

which it is possible to recognise a specific pattern. In fact, it is possible to detect the damage size and position with a good precision to confirm the damage detection ability of H-CFRP laminates. The damage, in fact, results to have an asymmetrical shape, matching the original PTFE patch shape.

- **SMA/CFRP leading edge LVI**

A real internal damaged area generated by a low velocity impact was studied. Leading Edge-SMA sample was manufactured with a double layer of SMA wires to improve the impact properties and to allow a damage detection using the in-situ thermal technique after impact. The impact energy used to test this sample was set to 15 J.

In order to understand the extension of damage and the distribution inside the structure, the multiplex configuration was performed. The thermal data collected by the thermal camera are reported in Figure 26 where the apparent temperature variation of laminate surface is shown. Wire 3 shows cold spots all along its path to represent the presence of damage on all its length; while other wires were used as reference since they are free from any discontinuities. In this case, the heatwave slows down due to delamination area where air is present. The different thermal properties affect that zone, changing the thermal diffusion in that specific area. In the other sample part, instead, the heatwave is free to spread uniformly in the sample: the difference between these two areas gives an indication about the structural integrity of the hybrid laminate.

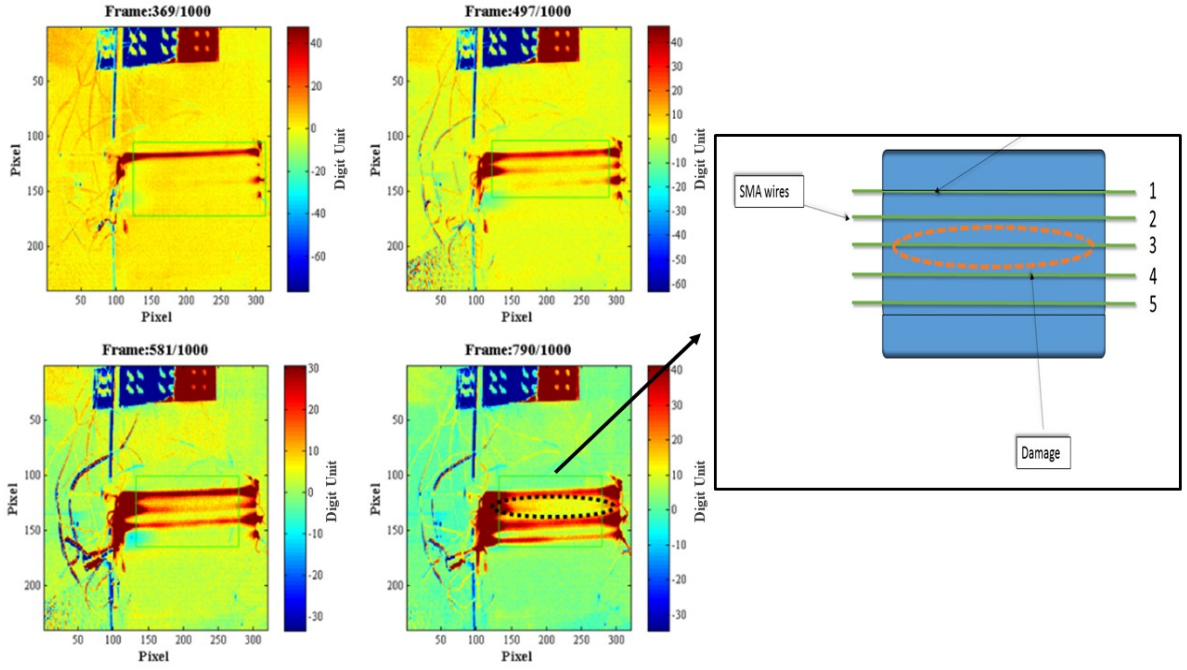

Figure 26 – Thermal images of Leading Edge SMA evaluated after the background subtraction procedure (multiplex configuration) with schematic layout of damaged area position.

In fact, the delaminated area is clearly detected in the central portion of the sample, where wire 3 is located.

4.4 De-Icing system

The proposed material concept de-icing capability was investigated exploiting the thermos-resistive properties of the embedded hybrid layer. In aeronautic, ice formation on the wing surface is a common problem and requires the use of external systems to defrost the concerned surface in order to avoid incidents or crashes [54]. In fact, if ice is allowed to build up to a significant thickness, it can change the shape of aerofoil and flight control surfaces, degrading the performance, control or handling characteristics of the aircraft as reported by Bragg and al. [55]. De-icing tests were conducted on a Leading edge SMA sample. The aim of this test is to carry out a feasibility investigation to understand the potentiality of the hybrid embedded system to be employed in de-icing applications. In Figure 27.a, the thermogram was reported in reference on a central spot of the sample where each curve was evaluated in a different instant of time.

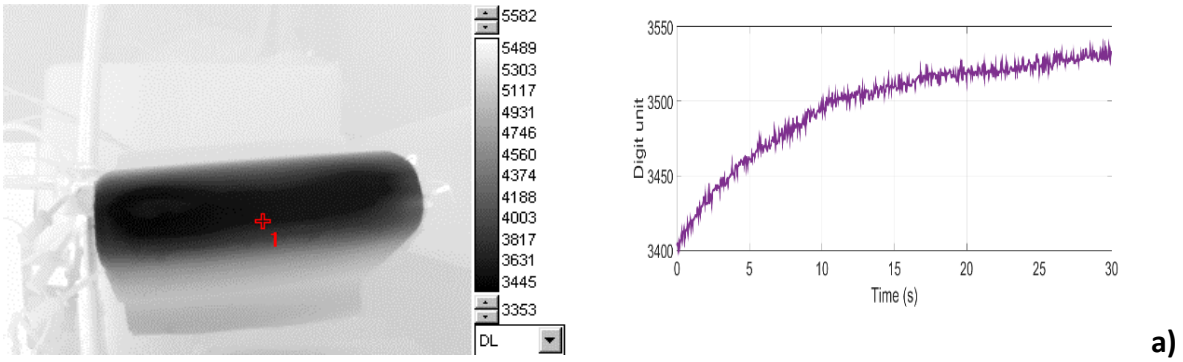

a)

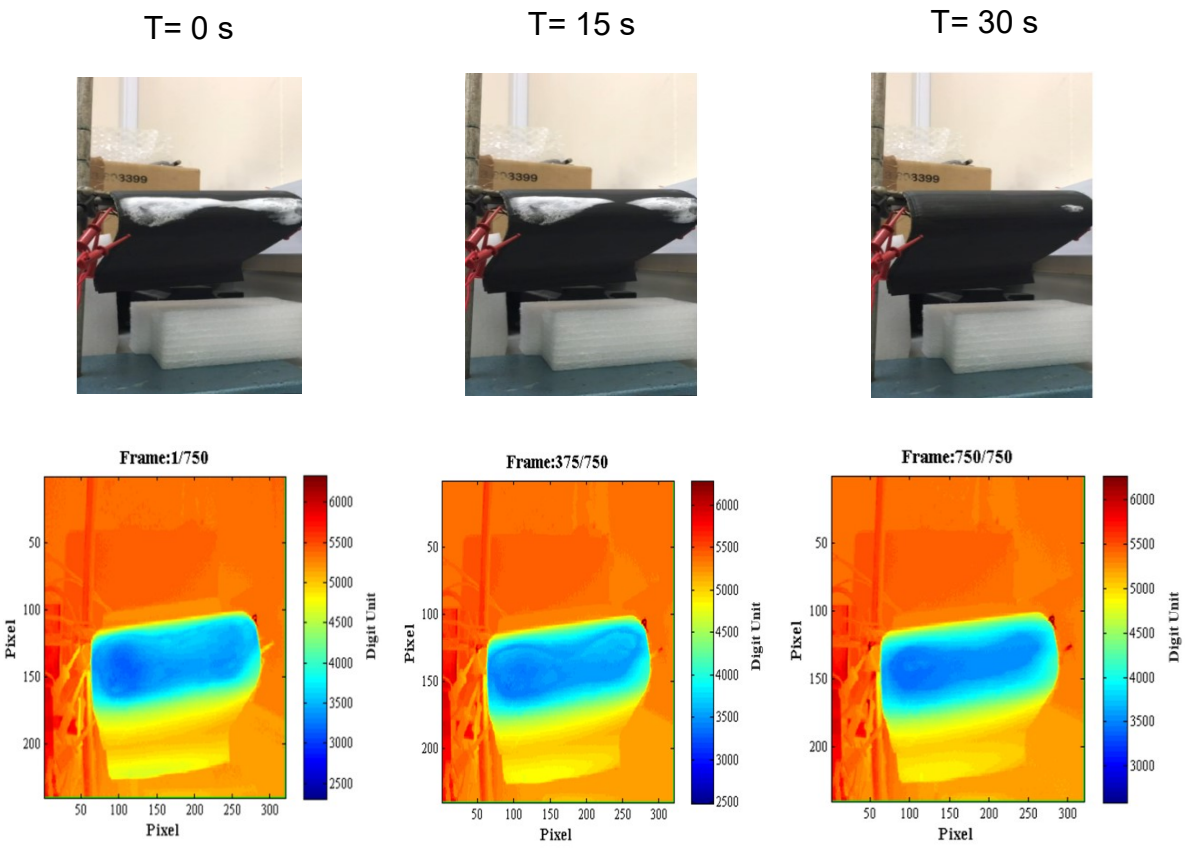

b)

Figure 27 -De -icing process on Leading Edge PTFE at different time steps: a)Thermogram of apparent temperature and b) relative thermal images reporting the ice dissolution

It is evident the validity of the procedure to melt down the ice on the sample surface as shown in Figure 27.b. During the scanning, wires generate heat that spreads out towards the surface. This process requires a certain time to be efficient, but it is still possible to see that the ice disappears efficiently even at 15 s from the beginning of the excitation. Afterwards, the single reference point chosen for the thermogram, due to ice melting, shows no further information regarding to the condition of the entire surface. In order to clarify the thermal distribution on whole sample surface, the apparent temperature was evaluated along two different lines: a horizontal and vertical one that crossed the reference points used in the previous tests. As shown in Figure 28, the apparent temperature results at minimum in both cases, at T=0 s, when the ice is present on the composite surface (blue curve). At T=15 s (yellow curve), the temperature increases due to wires heating. Along x-axis, its distribution remains congruent with the previous curve even if at higher temperature; while along the y-axis, apparent temperature increases more on the ends the sample than on the centre. At T= 30 s the ice is mostly dissolved on the entire sample. Along the x-axis the apparent temperature remains the same on the centre, but changes on the ends where sensibly increases. Along y-axis, instead, apparent temperature appears mostly the same even if increase slightly on the borders. The data shows an optimal behaviour in de-icing ability as ice is completely disappeared from sample surface in 30s of thermal excitation. Consequently, it is free from any defects that may cause interferences on the aerodynamic design. It is important to underline that the generated heat is directly proportional to the applied electrical current (temperature) and the time of activation. For instance, considering the experimental parameters used for a single wire, a voltage of 3.04 V and 0.55 A is applied in order to generate 1.67 W of thermal power *P* (Joule's effect). A preliminary estimation of the required deicing energy is calculated using the formula

$$Q_{tot} = Q_{lh} + Q_f = m_{ice}(C_{lh} + C_f(T_0 - T_f)) \quad (21)$$

where C_{lh} and C_f are ice the specific heat of fusion (333.55 kJ/kg) and specific heat capacity (4.18 kJ/(kg·K)) respectively, m_{ice} is the mass of the ice layer, T_0 is the initial temperature measured on the sample surface (-30°C) and T_f is the final temperature acceptable for deice requirements (+6°C) [56]. The mass of ice is calculated considering leading edge area extension of 0.015 m^2, thickness of 3 mm (volume of 4.5E-5 m^3) and ice density (0.92 kg/m^3). Using these values in equation 21, the resultant energy for deicing is estimated around 20 J/(kg·K). Considering the available thermal power and the required thermal energy for the deicing, the minimum time of activation t_{act} can be estimated using the formula:

$$t_{act} = \frac{Q_{tot}}{P}. \quad (22)$$

The time of activation of the system is then calculated and around 12 s are required for each wire to allow the leading edge surface to reach the optimal temperature and minimize the adhesion of the ice layer on sample surface allowing aerodynamic interactions to remove it [56]. According to this preliminary estimation, it is clear that the system can be tuned to generate the right amount of heat to deice the leading edge surface in function of the ambient conditions. Indeed, it is important to notice that for extremely cold environment (temperature lower than -30°C) in order to reach the optimal surface temperature and melt down the ice

layer, the deicing system has to be activated for a longer interval of time with an optimized current feed since mechanical properties could be locally affected by the temperature increase as already discussed previously. It is also important to underline that some operative parameters can influence this calculation including the distance between external surface of the component and the metal wires, since a shorter time interval is required to reach the melt-down temperature on the part. Following a different approach and applying a lower current for a longer time period, instead, it is possible to obtain a uniform temperature over all the surface that is potentially suitable during off-service schedule to avoid the ice formation on critical surfaces. In addition, the heating system also can be used to maintain an optimal constant temperature during in-service operations to prevent mechanical properties detriment due to low temperature [57-59]. Therefore, by carefully tuning the length of the excitation and the intensity of the current it is possible to generate an internal heatwave strong enough to melt ice formation while providing for a safety device to avoid the mechanical properties reduction in extremely cold environments.

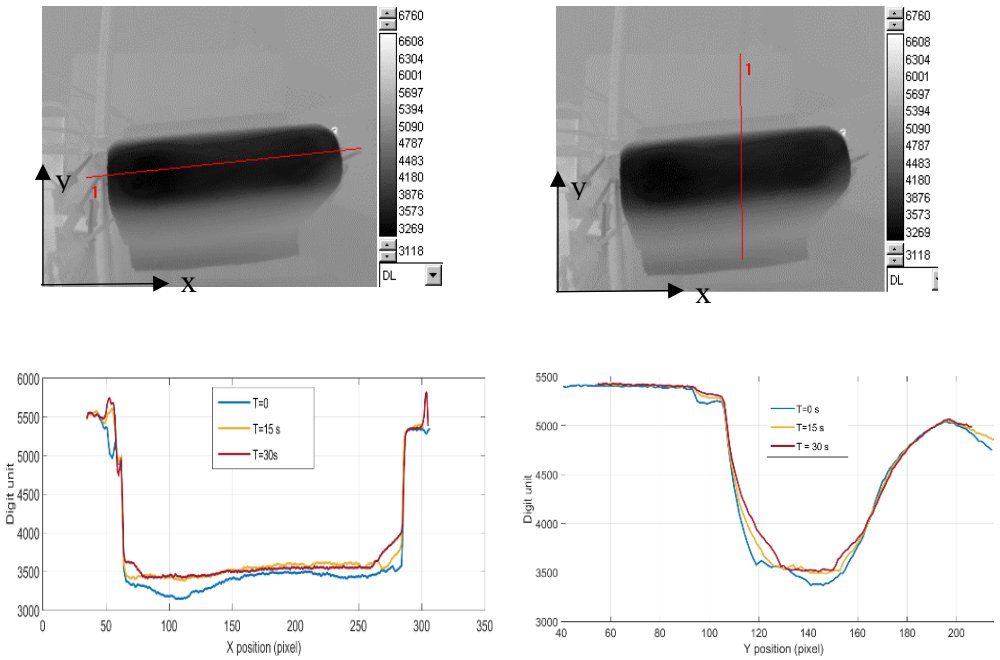

Figure 28 –Thermogram of apparent temperature along sample x-axis and y-axis.

5. Conclusions

This study proposes a smart multifunctional composite material where a hybrid phase (metal wires and carbon fibres) allows impact resistance enhancement, strain monitoring, damage detection and de-icing. Several typologies of samples were experimentally tested investigating the advantages of the smart network embedded within the CFRP. The effect of the hybridisation on the impact properties was investigated locating the metal array at different positions along the laminate's thickness and subjecting the samples to low-velocity impacts. A smaller delaminated area (-4%) were recorded with respect to a traditional CFRP when the hybrid phase was placed into the compressive portion of laminate with global weight increase only of 1%. The strain sensing ability was evaluated by measuring the electrical resistance variation of the array in presence of a distributed and a concentrated load. Both cases reported a congruent

correlation with the theoretical model and, in particular, in the concentrated case, it was possible to identify the specific point where the load was applied. Furthermore, once that the system records the evidence of an impact event, the presence of a damaged area can be identified within the laminate's body using Ir damage detection technique. The hybrid phase can be used as a heat source exploiting its thermo-resistivity via Joule effect by applying an electrical current on the wires, while an Ir camera records thermal data. The proposed approach allows scanning composite structures to detect delaminated areas, cracks or other BVIDs, while optimising power consumption and inspection time. Both simulated (PTFE patch) and real damage were successfully identified on both flat panels and leading edge geometries. Finally, de-icing capability was demonstrated. The results showed that it was possible to remove an ice layer from the leading edge surface by performing a thermal scanning of 30s and focusing the power only on the wires that surround the very edge of the sample using the multiplex system. The proposed smart material concept could improve the safety and reliability of aircraft structures and reduce maintenance costs.

Acknowledgements

This paper has been funded by the EXTREME project of the European Union's Horizon 2020 research and innovation programme under grant agreement No. 636549.

REFERENCES

[1] Abrate S. Impact on laminated composite materials. Appl Mech Rev. 1991;44:155-90.

[2] CHEN G, BIDINGER G, LOU M. IMPACT DEMAGE TOLERANCE OF THIN WALL COMPOSITE STRUTS. 34th Structures, Structural Dynamics and Materials Conference1993. p. 1398.

[3] Recker H. Highly damage tolerant carbon fiber epoxy composites for primary aircraft structural applications. 34 INTERNATIONAL SAMPE SYMPOSIUM AND EXHIBITION, 19891989. p. 747-58.

[4] Russell AJ, Street KN. The effect of matrix toughness on delamination: static and fatigue fracture under mode II shear loading of graphite fiber composites. Toughened composites: ASTM International; 1987.

[5] Tissington B, Pollard G, Ward I. A study of the impact behaviour of ultra-high-modulus polyethylene fibre composites. Composites Science and Technology. 1992;44:197-208.

[6] Yuan Q, Wu D, Gotama J, Bateman S. Wood fiber reinforced polyethylene and polypropylene composites with high modulus and impact strength. Journal of Thermoplastic Composite Materials. 2008;21:195-208.

[7] Ko FK, Hartman D. Impact behavior of 2-D and 3-D glass/epoxy composites. Materials Science for the Future: 31 st International SAMPE Symposium and Exhibition1986. p. 1272-84.

[8] Liu D. Delamination resistance in stitched and unstitched composite plates subjected to impact loading. Journal of Reinforced Plastics and Composites. 1990;9:59-69.

[9] Lopresto V, Melito V, Leone C, Caprino G. Effect of stitches on the impact behaviour of graphite/epoxy composites. Composites Science and Technology. 2006;66:206-14.

[10] Kim J-K, Sham M-L. Impact and delamination failure of woven-fabric composites. Composites Science and Technology. 2000;60:745-61.

[11] Ishai O, Shragai A. Effect of impact loading on damage and residual compressive strength of CFRP laminated beams. Composite Structures. 1990;14:319-37.

[12] Bunsell A, Harris B. Hybrid carbon and glass fibre composites. Composites. 1974;5:157-64.

[13] Naik N, Ramasimha R, Arya H, Prabhu S, ShamaRao N. Impact response and damage tolerance characteristics of glass–carbon/epoxy hybrid composite plates. Composites Part B: Engineering. 2001;32:565-74.

[14] Marom G, Drukker E, Weinberg A, Banbaji J. Impact behaviour of carbon/Kevlar hybrid composites. Composites. 1986;17:150-3.

[15] Vogelesang L, Marissen R, Schijve J. A new fatigue resistant material: Aramide Reinforced Aluminium Laminate (ARALL). 1981.

[16] Gunnink J, Vogelesang L, Schijve J. Application of a new hybrid material (ARALL) in aircraft structures. Proceedings of the 13th Congress of the International Council of the Aeronautical Sciences (ICAS), Washington1982. p. 990-1000.

[17] Vlot A. Glare: history of the development of a new aircraft material: Springer Science & Business Media, 2001.

[18] Vlot A, Gunnink J, Alderliesten R, Van der Hoeven W, de Boer A, Hart W, et al. Towards technology readiness of fibre metal laminates- Glare Technology Development(GTO) 1997-2000. ACUN- 3 International Composites Conference, Proceedings, Sydney, Australia, Feb 5-9, 2001, Sydney 2052, Australia, University of New South Wales, 20012001. p. 243-56.

[19] Bradley P, Harris S. Strategic reinforcement of hybrid carbon fibre-reinforced polymer composites. Journal of Materials Science. 1977;12:2401-10.

[20] Paine JS, Rogers CA. The response of SMA hybrid composite materials to low velocity impact. Journal of Intelligent Material Systems and Structures. 1994;5:530-5.

[21] Abry J, Bochard S, Chateauminois A, Salvia M, Giraud G. In situ detection of damage in CFRP laminates by electrical resistance measurements. Composites Science and Technology. 1999;59:925-35.

[22] Schulte K, Baron C. Load and failure analyses of CFRP laminates by means of electrical resistivity measurements. Composites Science and Technology. 1989;36:63-76.

[23] Cui D, Song G, Li H. Modeling of the electrical resistance of shape memory alloy wires. Smart Materials and Structures. 2010;19:055019.

[24] Nagai H, Oishi R. Shape memory alloys as strain sensors in composites. Smart Materials and Structures. 2006;15:493.

[25] Meola C, Carlomagno GM. Recent advances in the use of infrared thermography. Measurement science and technology. 2004;15:R27.

[26] Sakagami T, Kubo S. Applications of pulse heating thermography and lock-in thermography to quantitative nondestructive evaluations. Infrared Physics & Technology. 2002;43:211-8.

[27] Maierhofer C, Brink A, Röllig M, Wiggenhauser H. Transient thermography for structural investigation of concrete and composites in the near surface region. Infrared Physics & Technology. 2002;43:271-8.

[28] Suzuki Y, Todoroki A, Mizutani Y. Diagnosis for CFRP aircraft by Joule heating using lightning protection system. Proceedings of 12th Japan International SAMPE Symposium & Exhibition: Japan SAMPE; 2011.

[29] Ahmed T, Nino G, Bersee H, Beukers A. Heat emitting layers for enhancing NDE of composite structures. Composites Part A: Applied Science and Manufacturing. 2008;39:1025-36.

[30] Orłowska A, Kołakowski P, Holnicki-Szulc J. Detecting delamination zones in composites by embedded electrical grid and thermographic methods. Smart Materials and Structures. 2011;20:105009.

[31] Martin CA, Putt JC. Advanced pneumatic impulse ice protection system (PIIP) for aircraft. Journal of Aircraft. 1992;29:714-6.

[32] Graber DJ, Mack GJ. Acoustical anti-icing system. Google Patents; 1991.

[33] BOND T, Shin J. Results of Low Power Deicer tests on a swept inlet component in the NASA Lewis Icing Research Tunnel. 31st Aerospace Sciences Meeting1993. p. 32.

[34] Hydro M. Ice Storm Management of Overhead Lines. CEA Workshop, Ier1993.

[35] Yasui M, Maekawa K, Naganuma Y, Suzuki K, Kojima Y, Ando H. Removal of icy snow accumulation on the transmission line by applying LC-spiral rod. Fujikura Technical Review. 1987;16:26-33.

[36] Giamati MJ. Electrothermal de-icing system. Google Patents; 1997.

[37] Pinto F, Ciampa F, Meo M, Polimeno U. Multifunctional SMArt composite material for in situ NDT/SHM and de-icing. Smart Materials and Structures. 2012;21:105010.

[38] Chien A-T, Cho S, Joshi Y, Kumar S. Electrical conductivity and Joule heating of polyacrylonitrile/carbon nanotube composite fibers. Polymer. 2014;55:6896-905.

[39] Kernin A, Wan K, Liu Y, Shi X, Kong J, Bilotti E, et al. The effect of graphene network formation on the electrical, mechanical, and multifunctional properties of graphene/epoxy nanocomposites. Composites Science and Technology. 2019;169:224-31.

[40] Pinto F, Maroun F, Meo M. Material enabled thermography. NDT & E International. 2014;67:1-9.

[41] Ogisu T, Ando N, Takaki J, Okabe T, Takeda N. Improved Surface Treatment of SMA Foils and Damage Suppression of SMA-Foil Embedded CFRP Laminates. Journal of Intelligent Material Systems and Structures. 2001;12:265-70.

[42] Angioni SL, Meo M, Foreman A. Impact damage resistance and damage suppression properties of shape memory alloys in hybrid composites—a review. Smart Materials and Structures. 2011;20:013001.

[43] Yang R, Xu XS, Li KZ. The Influence of Metal Surface Roughness on Bonding Strength of Metal and Composite Material. Advanced Materials Research. 2015;1095:879-82.

[44] Kwon YS, Sankar BV. Indentation-flexure and low-velocity impact damage in graphite epoxy laminates. Journal of Composites, Technology and Research. 1993;15:101-11.

[45] Nettles AT, Douglas MJ. A comparison of quasi-static indentation to low-velocity impact. 2000.

[46] Hawileh RA, Abu-Obeidah A, Abdalla JA, Al-Tamimi A. Temperature effect on the mechanical properties of carbon, glass and carbon–glass FRP laminates. Construction and Building Materials. 2015;75:342-8.

[47] Wolfrum J, Eibl S, Lietch L. Rapid evaluation of long-term thermal degradation of carbon fibre epoxy composites. Composites Science and Technology. 2009;69:523-30.

[48] De Giorgi M, Nobile R. A possible use of SMArt thermography for the control of GFRP composite laminate. Procedia Structural Integrity. 2018;12:239-48.

[49] Wilson CD. Linear elastic fracture mechanics primer. 1992.

[50] Khalili S, Shokuhfar A, Ashenai Ghasemi F, Malekzadeh K. Dynamic response of smart hybrid composite plate subjected to low-velocity impact. Journal of composite materials. 2007;41:2347-70.

[51] Macaulay W. Note on the deflection of beams. The Messenger of Mathematics. 1919;48:129-30.

[52] Gibson RF. Principles of composite material mechanics: CRC press, 2016.

[53] Botelho EC, Silva RA, Pardini LC, Rezende MC. A review on the development and properties of continuous fiber/epoxy/aluminum hybrid composites for aircraft structures. Materials Research. 2006;9:247-56.

[54] COLE J, SAND W. Statistical study of aircraft icing accidents. 29th Aerospace Sciences Meeting1991. p. 558.

[55] Bragg M. Aircraft aerodynamic effects due to large droplet ice accretions. 34th Aerospace Sciences Meeting and Exhibit1996. p. 932.

[56] Meier O, Scholz D. A handbook method for the estimation of power requirements for electrical de-icing systems. DLRK, Hamburg. 2010;31.

[57] Sánchez-Sáez S, Gómez-del Rıo T, Barbero E, Zaera R, Navarro C. Static behavior of CFRPs at low temperatures. Composites Part B: Engineering. 2002;33:383-90.

[58] Nettles A, J. Biss E. Low Temperature Mechanical Testing of Carbon-Fiber/Epoxy-Resin Composite Materials1996.

[59] Zaoutsos S, Zilidou M. Influence of extreme low temperature conditions on the dynamic mechanical properties of carbon fiber reinforced polymers. IOP Conference Series: Materials Science and Engineering: IOP Publishing; 2017. p. 012024.